A Neuropeptidergic Signaling Pathway for Olfactory Gain Modulation

Tyler R. Sizemore[1,2]✉, **Julius Jonaitis**[1], **and Andrew M. Dacks**[1,3]

[1]Department of Biology, Life Sciences Building, West Virginia University, Morgantown, WV, 26506, USA
[2]Present Address: Department of Molecular, Cellular, and Developmental Biology, Yale Science Building, Yale University, New Haven, CT, 06520-8103, USA
[3]Department of Neuroscience, West Virginia University, Morgantown, WV, 26506, USA

Sensory systems are dynamically adjusted according to the animal's ongoing needs by neuromodulators, such as neuropeptides. Despite their prevalence across all nervous systems[1,2], how peptidergic neurons and the neuropeptide they release act to adjust sensory processing remains poorly understood. Here, we reveal that a heterogeneous ensemble of local interneurons (LNs) release the neuropeptide myoinhibitory peptide (MIP) within the *Drosophila* primary olfactory center (the antennal lobe, AL). We find MIPergic LNs form reciprocal connections with many AL principal neurons, but only a subset express the inhibitory MIP receptor (sex peptide receptor, SPR). We find both the MIPergic LNs and several of the SPR-expressing neurons are activated by the food-related odor apple cider vinegar (ACV), therefore suggesting MIP plays a role in adjusting ACV responses within the AL. We demonstrate that MIP can simultaneously decrease olfactory input to some glomeruli, while indirectly increasing olfactory input to others. As those glomeruli boosted by MIP – as well as MIP itself – are necessary and sufficient to initiate an attractive behavioral response to ACV[3,4], the neural substrates identified here may represent a key circuit element for the animal's switch in behavioral responses.

Neuromodulation | Neuropeptide | Olfaction | Connectomics | Local Interneuron | *Drosophila*

Correspondence: ***sizemoretyler92@gmail.com***

INTRODUCTION

Animals use their sensory systems to internalize and process information about the identity, intensity, and valence of external stimuli, so they can properly navigate their environment. However, constant ecological and internal state fluctuations threaten the animal's ability to accurately represent these stimuli. To address the demands these fluctuations impose, sensory systems use processes such as neuromodulation to flexibly adjust sensory processing and behavior. The largest and most ancient collection of neuromodulators are neuropeptides[1,5–13]. For instance, neuropeptide F (NPF)/neuropeptide Y (NPY) play a conserved role in promoting feeding behaviors in sea slugs, humans, flies, nematodes, mosquitoes, and rodents[14–21]. However, unraveling the circuit architecture of neuropeptide signaling within sensory modalities has proven difficult given limited knowledge of the structure and connectivity of many peptidergic neurons, as well as the inability to resolve the downstream peptide receptor-expressing neurons. As previously posited[22,23], these confounds have often meant our understanding of how neuropeptides act at the cellular level to adjust sensory processing remains ambiguous.

Here, we reveal a novel neuropeptidergic pathway within the *Drosophila* AL that modulates the gain of olfactory input to several food-odor associated channels. We show that the neuropeptide MIP is released by GABAergic LNs that as individual neurons innervate a different complement of glomeruli from animal-to-animal, but as an ensemble innervate all glomeruli across all animals. Through light- and electron-microscopy (EM) analyses, we show that these MIPergic LNs reciprocally communicate with an array of AL principal neurons. These anatomical connections are functionally tested by measuring MIPergic LN *in vivo* odor-evoked responses to a panel of diverse odorants. These recordings reveal that MIPergic LNs are consistently and robustly activated by the food-associated odor ACV. Moreover, we find that the inhibitory MIP receptor (SPR) is expressed by olfactory afferents (OSNs), projection neurons (PNs), and a few inhibitory LNs. More specifically, we find SPR is expressed by food-odor associated OSNs, and that MIP application directly reduces and indirectly increases the *in vivo* odor-evoked responses of food-odor responsive OSNs. Previous behavioral analyses found that MIP signaling was necessary and sufficient to stimulate the fly's drive towards food-odors[4]. Moreover, the activity of at least one of the OSN populations boosted by MIP application is linked to behavioral attraction to food-related odors. Taken together with our results, this suggests MIPergic AL LNs may represent one of several neural substrates that underlie a satiety driven switch in olfactory behavior.

RESULTS

Patchy GABAergic LNs release MIP within the AL. The neurites of the AL-associated MIPergic neurons are restricted to the AL, which suggests MIP is released from AL LNs[24]. The Drosophila AL houses ~200 LNs whose distinct roles in olfactory processing have been associated with their transmitter content and morphology[25-35]. For example, individual cholinergic AL LNs innervate many glomeruli and perform lateral excitation as a means for broadening odor representations in the AL[32,33,36,37]. To determine whether MIP-immunoreactive (MIP-ir) AL neurons belong to a known AL LN chemical class, we assessed the overlap of MIP-immunoreactivity with markers for the major *Drosophila* small-neurotransmitters[38] **(Figure 1A and Figure S1)**. We find that AL MIP-ir neurons do not overlap with choline acetyltransferase (ChAT) or vesicular glutamate transporter

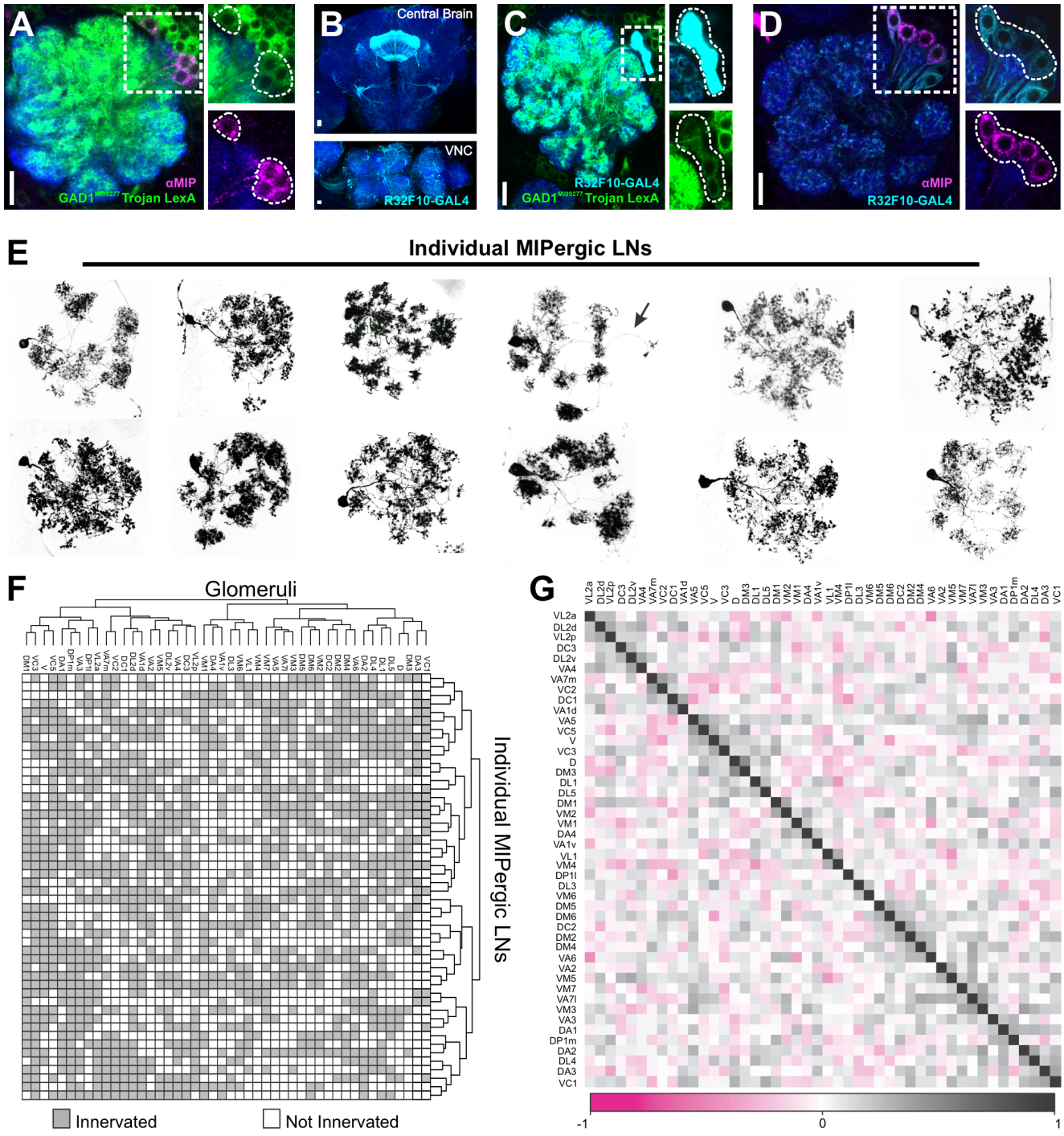

Fig. 1. Myoinhibitory peptide (MIP) is released by GABAergic patchy LNs in the AL. **(A)** A protein-trap Trojan LexA driver for glutamic acid decarboxylase (GAD1), the rate-limiting enzyme for GABA, highlights all MIP immunoreactive neurons in the AL. Cell counts: n = 5 brains, 10 ALs. **(B)** R32F10-GAL4 expression in the central brain and ventral nerve cord (VNC). **(C)** All R32F10-GAL4 AL LNs colocalize with the GAD1 Trojan LexA protein-trap driver. Cell counts: n = 5 brains, 9 ALs. **(D)** R32F10-GAL4 highlights ~13.2 (±0.68) AL neurons, which includes all MIP immunoreactive neurons (~8.7±0.3 neurons) and ~4.5 (±0.68) non-MIPergic LNs. Cell count estimates, n = 5 brains, 9 ALs. **(E)** Stochastic labeling of individual MIPergic LNs reveals MIP is released by patchy LNs. Arrow indicates a projection into the contralateral AL. **(F)** Glomerular innervation patterns of 50 individual MIPergic LNs organized by hierarchical clustering similarity. Each row represents the innervation pattern of a single MIPergic LN, and each column represents a given glomerulus. Note that in some cases a single MIPergic LN might project into the contralateral AL, but here only the ipsilateral innervation patterns were included for analysis. **(G)** All pairwise correlations of MIPergic LN innervation patterns between AL glomeruli. Values correspond to the Pearson's correlation coefficient for each glomerulus pair. In all cases: neuropil was delineated by anti-DN-Cadherin staining; scale bars = 10um.

(VGlut), but all MIP-ir neurons in the AL overlap with GAD1 (9.1±0.19 neurons, n = 5) **(Figure 1A and Figure S1)**. In accordance with RNA-sequencing[39–41], we find no detectable MIP-immunoreactive OSNs **(Figure S1)**. Altogether, these results suggest that GABAergic AL LNs release MIP within the AL.

The *Drosophila* AL houses a variety of distinct GABAergic LNs, which can be subdivided into five major morphological types: panglomerular, multiglomerular, oligoglomerular, continuous, and patchy[31]. Like cortical interneurons[42,43],

these different interneuron morphological types play distinct roles in AL olfactory processing. To determine which morphological type MIPergic LNs belong to, we screened the Janelia FlyLight driver line collection[44], tested ~25 of those lines for MIP-immunoreactivity, and identified a GAL4 driver (R32F10-GAL4) that selectively highlights MIPergic LNs within the AL **(Figure 1B-1D)**. We then used stochastic labeling[45] to resolve the morphology of individual MIPergic LNs, and found that all MIPergic LNs have a discontinuous innervation pattern resembling that of patchy AL LNs **(Figure 1E)**.

There are many AL neurons, including other LNs, that are not patchy LNs but resemble the discontinuous morphology described for patchy LNs[31]. However, individual patchy LNs are unique in that they innervate different sets of glomeruli from animal-to-animal[31]. Therefore, we analyzed the set of glomeruli innervated by 50 individual MIPergic LNs and observed 50 distinct innervation patterns, thus demonstrating that no individual MIPergic LN innervates the same set of glomeruli across animals **(Figure 1F and Figure S2 & S3)**. Additionally, we find individual MIPergic LNs do not preferentially innervate any one glomerulus over others **(Figure S2)**. When sister clones were assessed, we find that two individual MIPergic LNs co-innervate ~12 glomeruli (n = 5 brains, 5 sister clones) **(Figure S3A & S3B)**, and individual MIPergic LNs consistently innervated at least one of the hygro-/thermosensory associated glomeruli **(Figure S3C-E)**. These results suggest that at least two MIPergic LNs innervate any single glomerulus, including hygro-/thermosensory glomeruli[46–48]. Altogether, these observations confirm that MIPergic LNs are indeed patchy LNs that, as individual LNs, innervate different glomeruli from animal-to-animal.

Monomolecular odorants generally do not activate a single glomerulus[3,49–51]. Thus, if individual MIPergic LNs innervate different sets of glomeruli from animal-to-animal, are there pairs of glomeruli that are innervated significantly more than others? If so, what ecological relationships exist amongst significantly correlated pairs of glomeruli? Correlation analysis between pairs of glomeruli **(Figure 1G and Supplementary Table 1)** revealed several statistically significant relationships, of which the most significant pairs were DM3-D ($r = 0.49$, $p = 2.7 \times 10^{-4}$) and VL2p-VA6 ($r = -0.47$, $p = 4.9 \times 10^{-4}$). In addition to DM3-D and VL2p-VA6, this analysis also revealed a significant probability for MIPergic LN co-innervation amongst several pairs of glomeruli responsive to ACV[3], such as VM2-DM1 ($r = 0.35$, $p = 0.01$), DM4-DM2 ($r = 0.31$, $p = 0.03$), and DP1m-DM1 ($r = 0.29$, $p = 0.04$). This suggests that MIPergic LNs and/or MIP itself may play a vital role in modulating the balance of activity in ACV-responsive glomeruli.

MIPergic LNs Provide and Receive Broad Input and Output Across the AL. While no individual MIPergic LN innervates the same set of glomeruli from animal-to-animal **(Figure 2A)**, every glomerulus is innervated by at least one MIPergic LN across all animals **(Figure 2B)**. To determine if certain glomeruli contain substantially more MIPergic LN output than other glomeruli **(Figure 2C)**, we measured the density of MIPergic LN-expressed mCD8::GFP, anti-MIP immunoreactive puncta, and the synaptic polarity markers DenMark and synaptotagmin.eGFP (syt.eGFP)[52,53] in each glomerulus across many animals **(Figure 2D & 2E)**. We find that the density of each indicator varies across glomeruli but are stereotypic across samples **(Figure 2E and Figure S3F-I)**. The density of the output indicators (syt.eGFP and MIP-ir puncta) were statistically correlated, and nearly every indicator scaled with MIPergic LN intraglomerular cable density **(Figure S3F-I)**. Even so, we find within-indicator voxel densities are generally evenly distributed across each glomerulus, suggesting MIPergic LN input and output are evenly distributed across the AL **(Figure 2E)**.

These puncta analyses afford the advantages of analyzing MIPergic LN synaptic polarity across many individuals of both sexes. However, light microscopy is limited by its inability to resolve fine structures such as axons/dendrites[54,55]. Therefore, we sought to perform similar analyses on individual putative MIPergic LNs (putMIP LNs) within the densely-reconstructed hemibrain EM volume[56,57]. This allowed us to assess: (1) do certain glomeruli receive more input from putMIP LNs (and vice versa) than others? (2) what neurons are upstream/downstream of putMIP LNs in each glomerulus? and, (3) at which putMIP LN presynaptic terminals are vesicles associated with neuropeptides (dense core vesicles, or DCVs)[58,59] found? To do so, we first used several criteria **(see Methods)** for identifying fully-reconstructed putMIP LNs and identified 20 ideal candidates **(Figure 2F and Supplementary Table 1)**.

After identifying several optimal candidates, we wondered whether any putMIP LNs have distinct dendritic and axonic compartments. If true, this would suggest putMIP LNs make region-specific input/output not unlike the "heterogeneous LNs" in the honeybee AL[60–63]. Synaptic flow centrality and axonal-dendritic segregation indices[64] reveal all putMIP LNs lack clearly separable input/output compartments **(Figure 2F and Supplementary Table 1)**. When we assess the ratio of input-to-output along a given putMIP LN's intraglomerular neurites, we find that the amount of input a given putMIP LN receives typically outnumbers the amount of putMIP LN output within any given glomerulus **(Figure 2G)**. Therefore, we assessed the class and transmitter type of each presynaptic input an intraglomerular putMIP LN arbor receives to determine what may drive MIPergic modulation.

Generally, putMIP LNs receive more input from OSNs (45% of putMIP LNs; ~31-54% total input) than other principal neuron categories **(Figure 3A)**. Nearly 30% of putMIP LNs receive the majority of their input from PNs (~25-40% total input) and other LNs (~25% of putMIP LNs; ~26-41% total input) **(Figure 3A)**. Additionally, every putMIP LN forms strong connectivity with every other putMIP LN **(Figure 3A and Figure S3J-K)**. When the balance of excitatory, inhibitory, and modulatory input a given putMIP LN receives across all glomeruli is assessed, we find the amount of excitatory or inhibitory input a given putMIP LN receives varies greatly. Most putMIP LNs receive more excitatory than inhibitory input (~75-100% glomeruli innervated) **(Figure 3B)**.

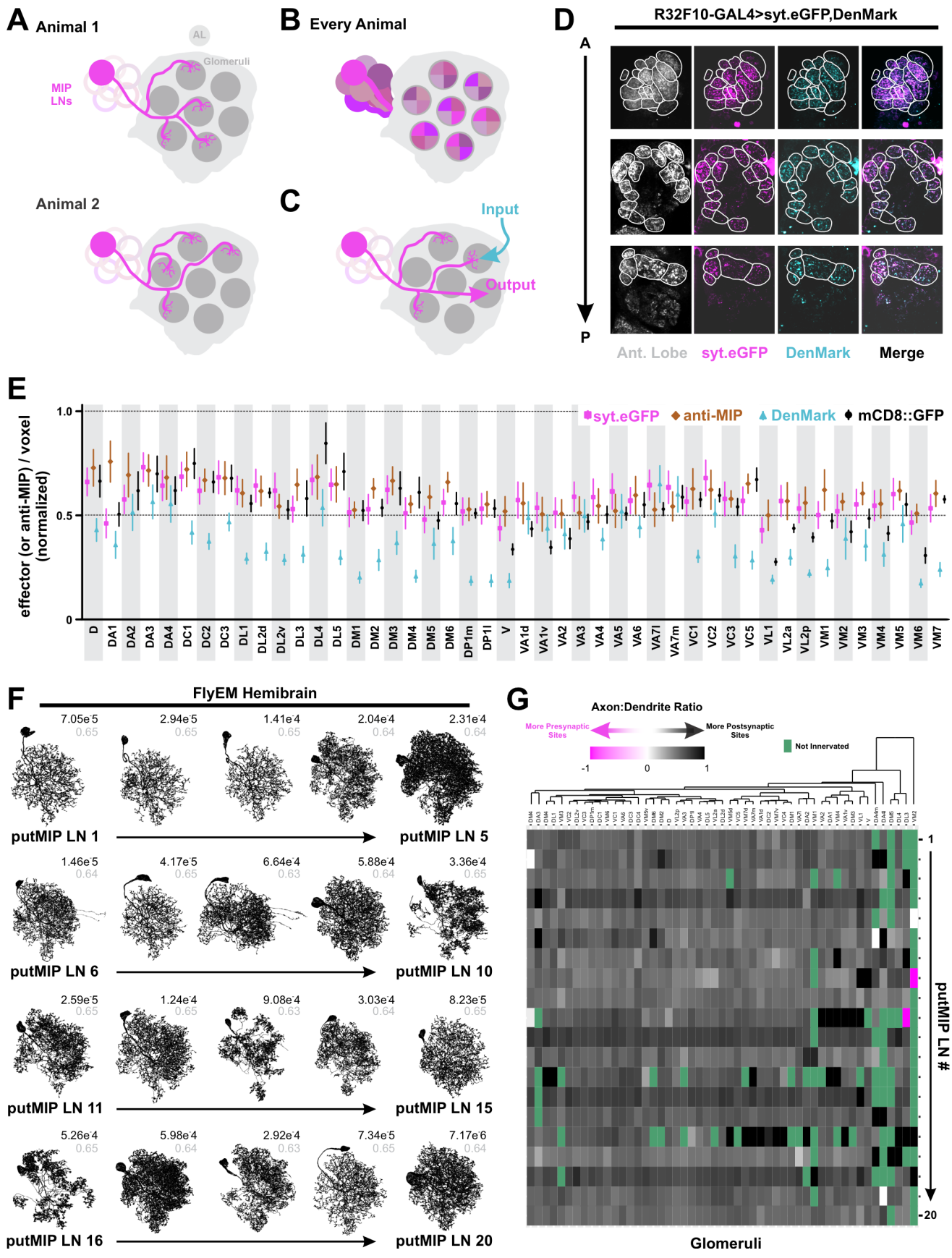

In some instances, the ratio of excitatory-to-inhibitory inputs were equal (10 glomeruli across 6 putMIP LNs), while in one case (putMIP LN 12 input in VM2) the ratio of all three input types were balanced **(Figure 3B)**. In one instance, the

Fig. 2. *Previous page.* **MIPergic LN input and output site throughout the entire AL. (A)** Individual MIPergic LNs project to different glomeruli from animal-to-animal. **(B)** The MIPergic LN ensemble covers the entire AL across all animals. **(C)** Do MIPergic LNs receive input from particular sets of glomeruli? Are there particular sets of glomeruli subject to more/less MIPergic LN output than others? **(D)** Representative image of glomerular voxel density analysis. Here, MIPergic LNs express synaptotagmin.eGFP (syt.eGFP; magenta) and DenMark (cyan) and their respective density is measured within each AL glomerulus (Ant. Lobe; grey). Glomeruli outlined in white. **(E)** syt.eGFP (magenta), DenMark (cyan), mCD8::GFP (black) and anti-MIP (brown) puncta density per voxel within each AL glomerulus. Each indicator is normalized to the highest value within that indicator. Data are represented as the mean±SEM of each indicator's voxel density within a given glomerulus. For each indicator, n = 7 (syt.eGFP), 7 (DenMark), 4 (mCD8::GFP), 4 (anti-MIP) brains. **(F)** Putative MIPergic LN (putMIP LN) mesh skeletons identified from the FlyEM FIB-SEM hemibrain connectome volume. For each neuron, values in the upper right-hand corner are that neuron's synaptic flow centrality index (black) and GMR32F10-GAL4 NBLAST similarity score (grey). **(G)** putMIP LN intraglomerular axon:dendrite ratio across the AL. Each column represents a given glomerulus, and each row represents the axon:dendrite ratio of a single putMIP LN. Glomeruli not innervated by the given putMIP LN are green. Glomeruli are organized by hierarchical clustering similarity. Data only consider putMIP LN connections within the ipsilateral AL.

amount of excitatory and modulatory input the intraglomerular putMIP LN arbor receives is equal (putMIP LN 5 in VM2) **(Figure 3B)**. Regardless, the amount of excitatory input generally dominates (~1.2-2.5x more) **(Figure 3B)**, which suggests MIPergic LNs may be broadly activated.

Synapse counts have been shown to strongly predict functional output strength in neurons within other systems, including other *Drosophila* AL neurons[26,65–70]. Hence, we hypothesized MIPergic LNs would be broadly activated by diverse odors, as intraglomerular putMIP LN arbors generally receive mostly excitatory input within a given glomerulus **(Figure 3B)**, However, *in vivo* MIPergic LN odor-evoked responses to a panel of chemically diverse odors revealed that most odors drive intraglomerular inhibitory responses in MIPergic LN neurites, regardless of behavioral valence **(Figure 3C-3E)**. For example, geranyl acetate and 1-octen-3-ol are respectively appetitive and aversive[71], but both odors evoke inhibitory responses in MIPergic LN neurites in DM5, DP1m, and VA2 **(Figure 3C-3E)**. In contrast, ACV reliably and consistently activated MIPergic LN neurites in every identifiable glomerulus **(Figure 3C & 3D)**. These results, together with our observations that multiple ACV-responsive glomeruli are statistically likely to be co-innervated by a single MIPergic LN **(Figure 1F)**, further suggests that MIP signaling likely plays a role in ACV processing.

MIPergic LN Downstream Partners and Widespread SPR Expression Within the AL. To determine the AL principal neurons likely targeted by MIPergic LNs, we first assessed the general output demographics for each putMIP LN **(Figure 4A & 4B)**. Most putMIP LNs target other non-putMIP LNs (45% of putMIP LNs; ~27-40% of total output) and OSNs (35% of putMIP LNs; ~28-44% of total output) **(Figure 4A)**. Since AL LNs express $GABA_A$ receptors[25], these results would suggest that MIPergic LNs may provide fast-acting disinhibition across the AL. To determine which of these downstream partners **(Figure 4B)** are likely targeted by MIPergic modulation, we determined which postsynaptic partners were downstream of putMIP LN terminals where DCVs are observable **(Figure 4C)**. We observed several instances where DCVs could be found in putMIP LN terminals presynaptic to OSNs, PNs, and ventral LNs **(Figure 4C)**. However, MIPergic LNs could also release other neuropeptide(s) that cannot be labeled for, so the presence of DCVs in MIPergic LN presynaptic terminals does not necessarily mean the downstream neuron is modulated by MIP. Moreover, putMIP LN EM analyses indicate several AL principal neuron types are plausible targets for MIPergic modulation **(Figure 3, Figure 4, and Figure 5A)**. To determine which downstream partners are subject to MIPergic modulation, we identified the AL neurons that express MIP's cognate receptor, the inhibitory SPR receptor[72–75]. To do so, we used a CRISPR/Cas9-mediated T2A-GAL4 insertion within the endogenous SPR locus to enable GAL4 expression within SPR-expressing cells[76] **(Figure 5B)**.

In *Drosophila*, OSN somata are located within the third-antennal segment and maxillary palp[77,78]. We find 208.9±11.89 (n = 17 animals, 30 antennae) and 63.42±4.31 (n = 18 animals, 31 maxillary palps) SPR-T2A-$GAL4^+$ neurons in the third-antennal segment and the maxillary palp, respectively **(Figure 5C & 5D)**. The number of SPR-T2A-$GAL4^+$ neurons in either appendage do not significantly differ based on the animal's sex or mating status (antennae: p = 0.107, one-way ANOVA; maxillary palps: p = 0.559, Kruskal-Wallis test). Through stochastic labeling experiments where the antennal nerve is left attached to the brain, we found OSN fibers that innervate many distinct glomeruli, including several ACV-responsive OSNs **(Figure 5E)**. Interestingly, we found SPR-T2A-GAL4 expression in afferents belonging to every sensory modality **(Figure S4)**, which suggests MIPergic modulation of sensory afferents may be a fundamental feature in *Drosophila*.

Within the brain, we noted overlap between SPR-T2A-GAL4 and the glial marker *reverse polarity* (REPO) **(Figure 5F)**, which we found correspond to: (1) cortical glia, (2) neuropil ensheathing glia, and (3) tract ensheathing glia **(Figure 5G)**. However, there is no evidence directly linking the actions of these glial subtypes with AL processing[79–81], so we turned our attention to SPR-T2A-GAL4 cells immunopositive for the proneural gene *embryonic lethal abnormal vision* (ELAV) **(Figure 5H)**. Through intersectional genetics and stochastic labeling, we find that these neurons consist of: 4.89±0.21 (n = 23) SPR-expressing ventral glutamatergic LNs (GlutLNs) **(Figure 5H & 5I)**, uniglomerular PNs **(Figure 5J)**, and several lateral LNs **(Figure 5K)**. In agreement with these results, we find similar neuron types using another SPR driver (SPR-GAL4::VP16)[82] **(Figure S5)**, publicly available scRNA-seq datasets[83–85] **(Figure S6)**, and a novel $SPR^{MI13553}$-T2A-LexA::QFAD driver **(Figure S7)**.

MIPergic Signaling Adjusts Afferent Gain in Food Odor-Associated Glomeruli. We have shown: (1) MIPergic LNs significantly co-innervate several ACV-responsive glomeruli **(Figure 1F)**; (2) putMIP LNs form many reciprocal connections and receive significant excitation within ACV-responsive glomeruli **(Figure 3B and Figure 4B)**; (3)

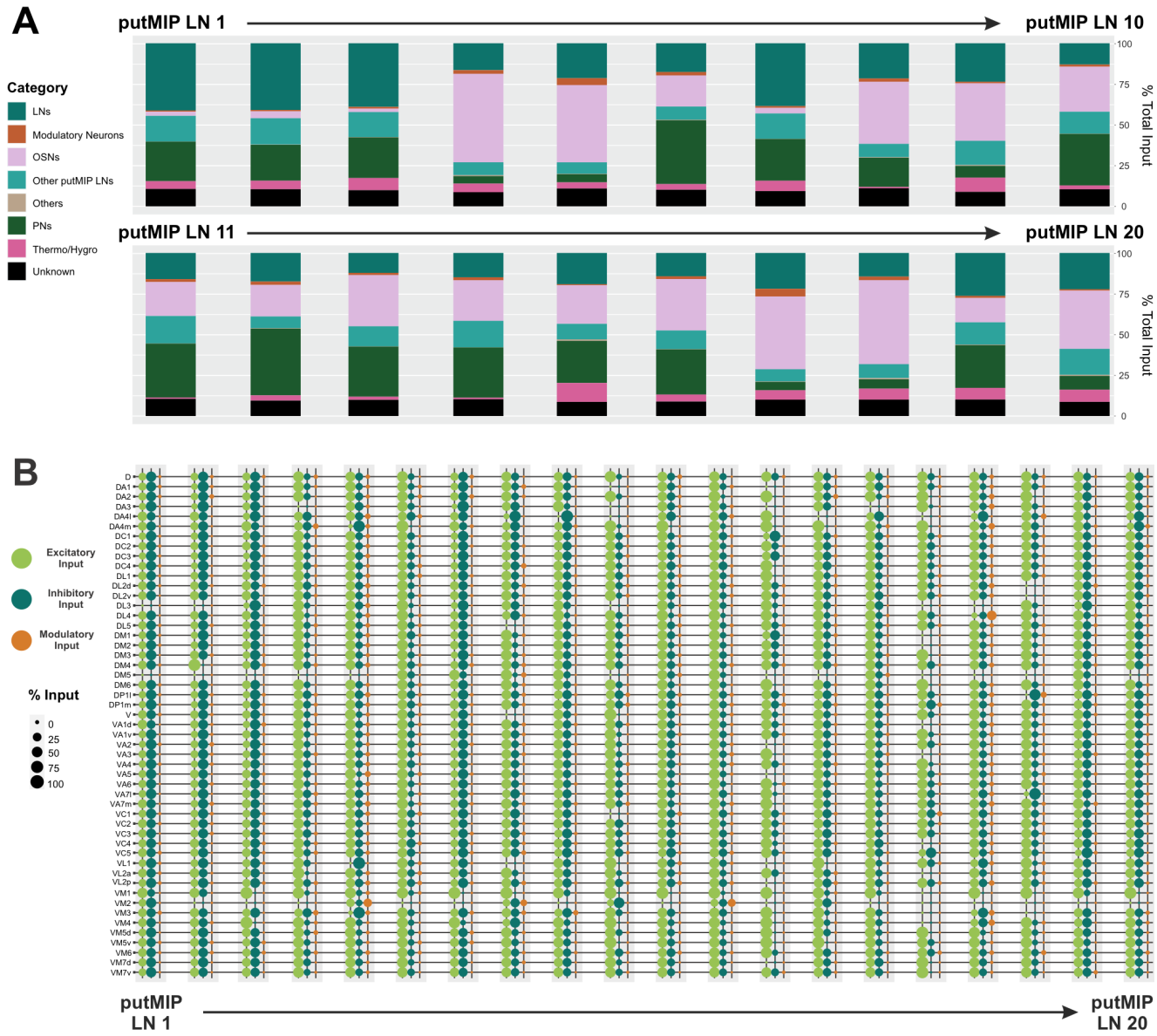

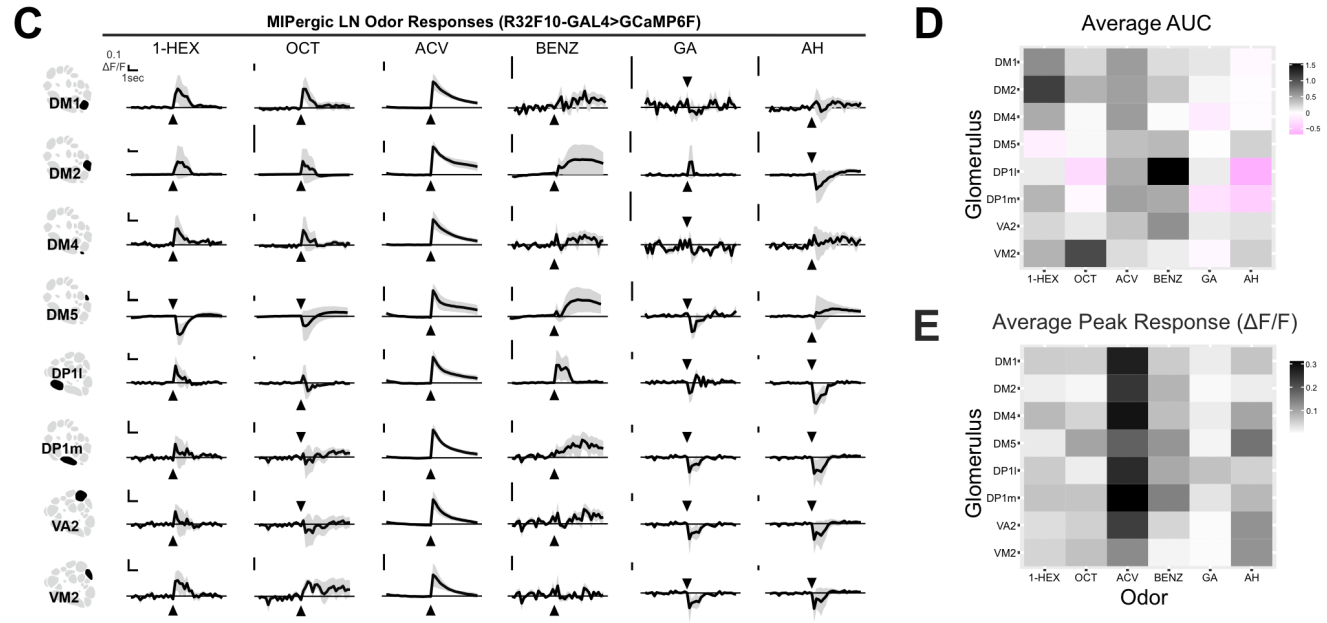

Fig. 3. *Previous page.* **Anatomical inputs to putMIP LNs and functional glomerular outputs from identified MIPergic LNs.** **(A)** putMIP LN upstream partners' demographics. Data are represented as a function of the total amount of input a putMIP LN receives from all categories. **(B)** The amount of excitatory, inhibitory, and modulatory input each putMIP LN receives within every glomerulus as a function of the total amount of input a given putMIP LN receives within the glomerulus. **(C)** Odor-evoked responses of MIPergic LN neurites within several AL glomeruli (far left column). Odors tested were presented at 10^{-2} and include: 1-hexanol (1-HEX), 1-octen-3-ol (OCT), apple cider vinegar (ACV), benzaldehyde (BENZ), geranyl acetate (GA), and ammonium hydroxide (AH). For each stimulus: n = 3-10 animals; vertical and horizontal scale bars = 0.1 ΔF/F & 1 second (respectively). Glomerular schematics derived from an *in vivo* AL atlas[151]. **(D)** Average area under the ΔF/F curve (AUC) of MIPergic LN neurites across glomeruli for each stimulus. **(E)** Average peak response (ΔF/F) of MIPergic LN neurites from odor onset to ~1 second after stimulus onset.

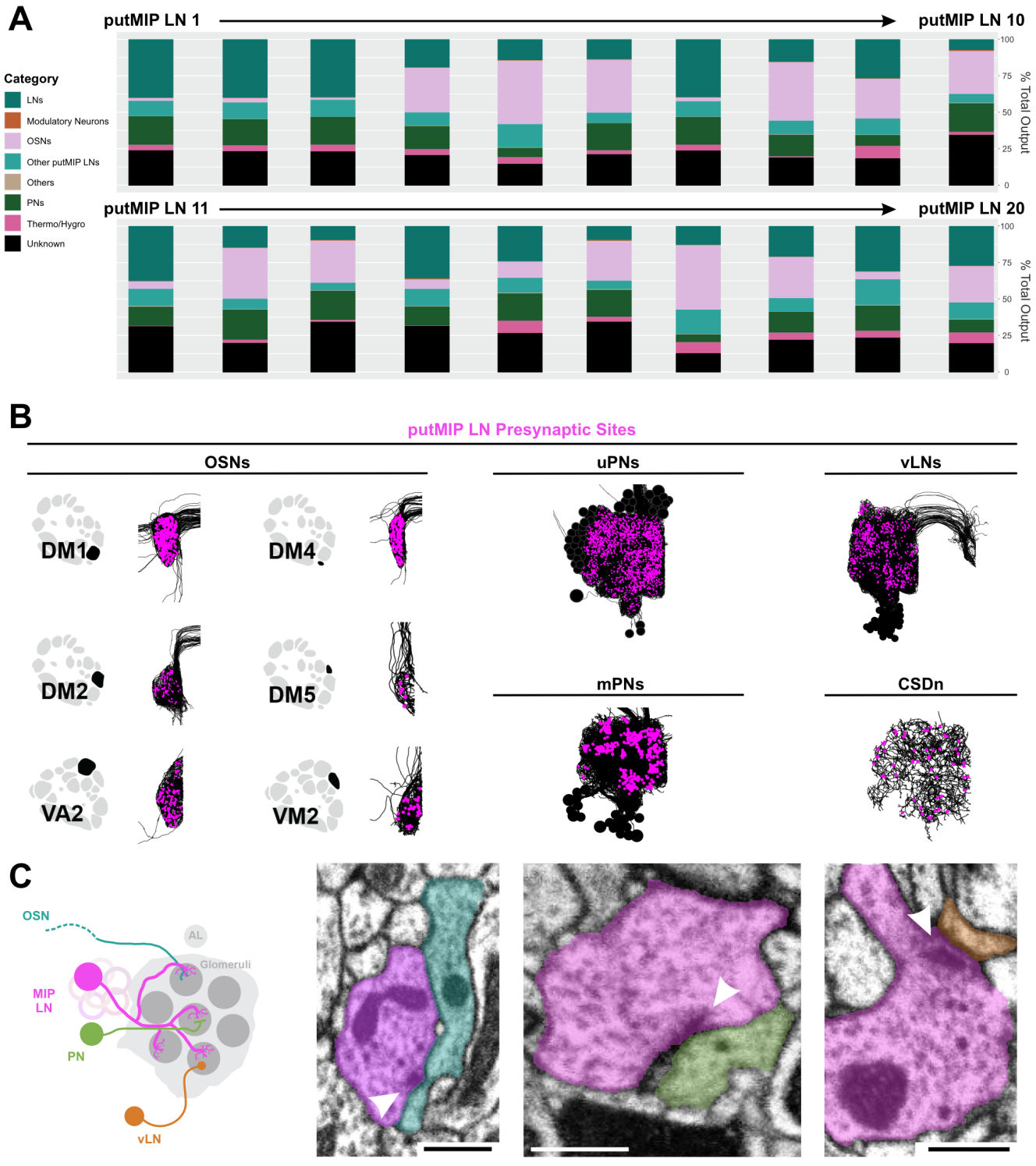

MIPergic LNs are consistently activated by ACV (**Figure 3C-3E**); and, (4) many ACV-responsive OSNs express the MIP receptor, SPR (**Figure 6A & 6B**). Altogether, these results indicate that ACV-responsive glomeruli are likely influenced by MIPergic modulation. To test whether MIP can alter the odor-evoked responses in ACV-responsive glomeruli,

Fig. 4. Postsynaptic targets of each putMIP LN and representative putMIP LN presynaptic terminals with dense core vesicles (DCVs). **(A)** Demographics of all putMIP LN postsynaptic targets by neuron type. Data are represented as a function of the total amount of output a putMIP LN sends to all categories. **(B)** putMIP LN postsynaptic partner skeletons (black) with putMIP LN presynaptic locations (magenta). Glomerular schematics derived from an *in vivo* AL atlas[151]. **(C)** Representative instances where DCVs in the putMIP LN presynaptic terminal. From left to right: DCVs are in putMIP LN presynaptic terminals upstream of OSNs (cyan), PNs (green), and ventral LNs (vLN; orange). In all cases: white arrowheads indicate the putMIP LN's presynaptic site; scale bars = 500nm.

we first recorded from the OSNs in these glomeruli before ("PRE"), during ("MIP"), and after applying synthetic MIP (synMIP) ("POST") **(see Methods) (Figure 6C)**. We chose to use this approach, as opposed to stimulating MIPergic LNs while recording from OSNs, to avoid misattributing observed effects to MIPergic LN release of MIP when GABA release is equally likely **(Figure 1A)**.

Olfactory sensory neuron axons robustly respond to both test concentrations of ACV before synMIP application ("PRE"), then after synMIP was pressure injected into the AL ("MIP") DM1 OSN responses to 10^{-2} ACV are increased **(Figure 6D)**. Similarly, DM4 OSN responses to 10^{-6} ACV are also increased after peptide application **(Figure 6E)**. After the washout period ("POST"), DM1 OSN responses to 10^{-2} ACV return to those akin to pre-peptide application responses **(Figure 6D)**, whereas the increased DM4 OSN responses to 10^{-6} ACV are sustained **(Figure 6E)**. In contrast, DM2 OSN responses are substantially diminished after peptide application regardless of odor concentration, and remain so post-washout **(Figure 6D & 6E)**. Moreover, DM5 OSN responses to 10^{-2} ACV, which were decreased (albeit insignificantly) upon peptide application, become significantly diminished post-washout relative to pre-peptide application **(Figure 6D)**. The observed decrease in DM2 and DM5 OSN responses are consistent with SPR expression in these OSNs **(Figure 5G)**. Altogether, these results show that MIP can differentially modulate OSN odor-evoked responses in a glomerulus- and stimulus-dependent manner, while also having stimulus-independent consequences on OSNs of another glomerulus. However, we acknowledge these observations may arise from polysynaptic influences induced by MIP application. Therefore, we decreased SPR levels in these OSNs to test the necessity of direct MIP-SPR signaling on the observed changes in OSN odor-evoked responses **(Figure 6F & 6G)**.

We find that SPR knockdown in DM2 and DM5 OSNs abolishes the MIP-induced decrease in each glomerulus' odor-evoked responses **(Figure 6F & 6G)**. This result is consistent with SPR-expression in DM2 and DM5 OSNs, and suggests MIP directly decreases the gain of DM2 and DM5 OSN responses. In contrast, SPR knockdown in DM1 and DM4 OSNs does not prevent their responses from increasing after peptide application **(Figure 6F & 6G)**. Since we did not observe SPR-expression in DM1 and DM4 OSNs **(Figure 5)**, and SPR knockdown in these OSNs does not abolish MIP-induced increase in their responses **(Figure 6F & 6G)**, these results suggest MIP acts polysynaptically to increase the gain of DM1 and DM4 OSN responses.

DISCUSSION

Our data reveal a novel neuropeptide signaling pathway that mediates olfactory gain control. We have shown that MIP is released by patchy GABAergic LNs that – as individuals – innervate a different complement of olfactory channels from animal-to-animal. However, these MIPergic LNs reliably innervate all glomeruli across all animals, where they receive and target many principal neuron types. We reveal all MIPergic LN downstream partners and show many principal AL neuron types express SPR and are therefore subject to MIPergic modulation. By testing MIP's effect on the odor-evoked responses of OSNs in several food-odor associated glomeruli, we reveal that MIP can have complex effects on OSN input to a glomerulus. For example, MIP directly decreases DM2 and DM5 OSN responses in an odor-concentration independent and dependent manner, respectively **(Figure 6)**. Moreover, we find that MIP indirectly increases DM1 and DM4 OSN input in a concentration dependent manner **(Figure 6)**. As the activity of these OSNs, and MIP itself, play a key role in the animal's odor-evoked behavioral responses[3,4,86], the neuropeptidergic pathway detailed here likely represents a key circuit switch for initiating olfactory behavioral attraction.

Generally, multiple glomeruli are activated by a given odorant[3,49–51,87]. To evaluate the behavioral contribution of individual glomeruli, "optogenetic odors" can be used to selectively activate individual glomeruli in a manner similar to their odor-evoked responses[86]. These experiments found that DM1 and DM2 coactivation do not summate, and co-stimulation of both glomeruli produces a behavioral response that resembles DM1-only activation[86]. Based on this, the investigators proposed that an antagonistic relationship exists between DM1 and DM2, such that co-stimulation reduces the efficacy of either or both glomeruli[86]. We find MIP indirectly increases DM1 and directly decreases DM2 OSN responses **(Figure 6)**. Therefore, MIP-SPR signaling in DM1 and DM2 may act as a homeostat such that coactivation of each glomerulus never produces a behavioral response greater than the DM1-only activation response. This "buffer" would be advantageous for preventing saturation at the downstream neurons that receives convergent input from these glomeruli[26,66,88,89].

We found that individual MIPergic LNs innervate a different repertoire of glomeruli across animals and do not preferentially innervate any one glomerulus over others **(Figure 1 and Figure S2)**. These findings are consistent with earlier reports wherein patchy AL LNs were first generally described[31]. But, what factor(s) give rise to the tremendous flexibility within this single morphological subtype? One explanation might be that MIPergic LN morphological idiosyncrasy is a byproduct of experience during development. Consistent with this, the initial LN glomerular innervation and dendritic elaboration during development requires OSN axons and cell-to-cell interactions[31,90]. However, OSN removal in the adult does not disrupt the animal-to-animal variability of patchy LNs[31]. To the best of our knowledge, a single

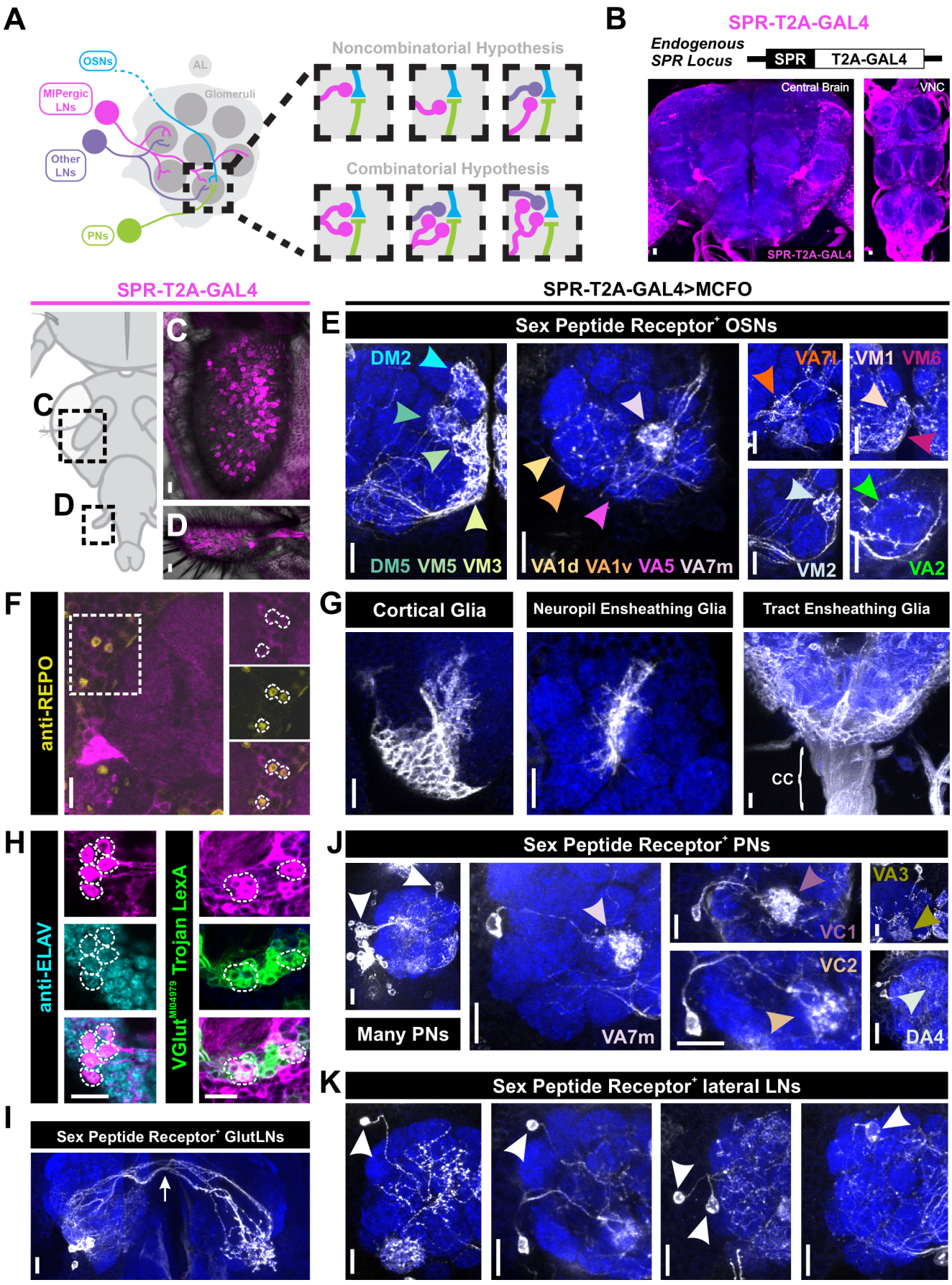

Fig. 5. *Previous page.* **Widespread sex peptide receptor (SPR) expression throughout the AL. (A)** MIPergic LNs (magenta) form synaptic connections with all principal neuron types in the AL; OSNs (cyan), PNs (green), and other LNs (purple). Therefore, within a single glomerulus, MIPergic modulation might target any one of these neuron types ("Non-combinatorial Hypothesis"), or multiple neuron types ("Combinatorial Hypothesis"). **(B)** SPR expression (magenta) revealed through a CRISPR/Cas9 T2A-GAL4 insertion in the SPR-coding intron. **(C D)** SPR-T2A-GAL4 expression in OSNs in the third-antennal segment and maxillary palp. **(E)** SPR-T2A-GAL4 stochastic labeling experiments where the antennal nerve remains intact reveals SPR-expressing OSNs project to: DM2, DM5, VM5v, VM5d, VM3, VA1d, VA1v, VA5, VA7m, VA7l, VM1, VM6, VM2, and VA2. **(F)** SPR-T2A-GAL4 colocalizes with the glial marker REPO (yellow). **(G)** SPR-T2A-GAL4 stochastic labeling reveals expression in cortical, neuropil ensheathing, and tract ensheathing glia. "CC" = Cervical Connective. **(H)** Several SPR-T2A-GAL4 neurons are immunopositive for the proneural marker ELAV (cyan), a subset of which colocalize with $VGlut^{MI04979}$ Trojan LexA (green). **(I)** SPR-T2A-GAL4 stochastic labeling reveals several bilaterally-projecting ventral glutamatergic LNs (GlutLNs). White arrow = bilateral projection. **(J)** Several lateral and anterodorsal PNs (white arrowheads) are highlighted via SPR-T2A-GAL4 stochastic labeling, some of which project to: VA7l, VC1, VC2, VA3, and DA4. **(K)** Approximately five lateral LNs are identified through SPR-T2A-GAL4 stochastic labeling. In all cases: neuropil was delineated by anti-DN-Cadherin staining; scale bars = 10um.

locus (e.g., environmental experience or heritable trait) that would support animal-to-animal variation in patchy LNs has not been identified. A pair of sexually-dimorphic ventral AL LNs ("TC-LNs") were recently shown to display an analogous idiosyncratic morphology phenotype which correlates with the animal's sex, mating status, and food ingestion[91]. These factors may similarly influence MIPergic LN variability, however we did not observe differences in the total number of MIPergic LNs based on sex or mating status (**Figure S1**), or sexual dimorphism in MIPergic LN synaptic polarity marker density (syt.eGFP: $p = 0.0634$; DenMark: $p = 0.4347$; $n = 3$ males, 4 females; two-way ANOVA).

Another explanation for animal-to-animal differences in individual MIPergic LN morphology is that it may not matter which individual MIPergic LN forms synapses with which downstream target, as long as all of the MIPergic LN downstream targets are met. Every nervous system is the byproduct of the adaptive pressures demanded by the animal's niche; a place that can continually change in seemingly unpredictable ways. Therefore, a developmental "parameter space" may exist, wherein just enough genetic idiosyncrasy is allowed to help prevent extinction in the face of environmental perturbations. The breadth of this developmental parameter space (or the degree of variability from the "median") would be defined by many generations of selective pressures, wherein subtle changes in genetic idiosyncrasies might equally result in winners and losers. As a consequence of these genetic idiosyncrasies, phenotypic variability in a given developmental program would inevitably accumulate, resulting in the observed animal-to-animal variability in neuronal features (e.g., morphology, ion channel distribution, etc.). Consistent with this idea, animal-to-animal variations in neural circuitry have been noted in grasshoppers[92], crabs[93–97], lobsters[98,99], flies[31,100,101], and rats[102]. Moreover, inter-animal variations in neuronal architecture are one of several features implicated in inter-animal behavioral variations[101,103–106,108]. However, despite this variability, overall neuronal circuit functions persist – such as the consistent MIP-induced decrease in DM2 and DM5 OSN responses (**Figure 6**). Moreover, several positive and negative correlations exist for pairs of glomeruli innervated by single MIPergic LNs, such as the significant probability for MIPergic LN co-innervation in ACV-responsive glomeruli (**Figure 1 and Supplementary Table 1**). This suggests that the morphology of an individual MIPergic LNs can differ from animal-to-animal, as long as the right combinations of downstream targets (e.g., food-odor responsive neurons) are met by the ensemble.

MIP-SPR signaling has been implicated in several behavioral state switches[4,107]. Notably, abolishing MIP release by inactivating all MIPergic neurons, or using a MIP-genetic null background, increases the animal's drive for food-derived odors[4]. Moreover, single sensillum recordings from DM2 OSNs displayed an increased firing rate when all MIPergic neurons are inactivated[4]. In contrast, increasing the activity of all MIPergic neurons decreases attraction toward food-odors, to the extent of eliciting odor-induced aversion[4]. Together, these behavioral results suggest MIP-SPR signaling controls the sensitivity to food-associated odors and drive to search for food. In accordance with these observations, we found that individual MIPergic LNs significantly co-innervate several food-odor associated glomeruli (**Figure 1**) and neurons from several of these glomeruli express the MIP receptor, SPR (**Figure 5**). Most strikingly, we find that MIP directly acts on DM2 OSNs to decrease the gain of their responses (**Figure 6**). Furthermore, we show that the MIP-induced decrease in DM2 responses occurs in a stimulus-concentration independent manner (**Figure 6**). Altogether, these results point to a probable role for MIPergic LN-derived MIP signaling to adjust olfactory processing, likely while other MIPergic neurons adjust other sensory/motor elements, in accordance with satiety homeostasis drives. However, this role is likely only one of many that the MIPergic LNs play in AL processing as they also release GABA, and form reciprocal connections with neurons outside of the SPR-expressing neurons (**Figure 3 & 4**).

Peptidergic modulation can be as simple as a single neuropeptide modulating motor output[109], or as complex as the ~37 neuropeptide families in the cortex[110]. Our data highlight how even a seemingly simple case (a single neuropeptide) can have complex consequences on network processing by acting non-uniformly within different components of the overall network. As neuropeptide functions are often deeply conserved, and as the actions of neuropeptides begin to come into focus, similar instances of complex and non-uniform peptidergic modulation will likely appear across disparate taxa and modalities.

ACKNOWLEDGEMENTS

We are grateful to Kristyn Lizbinski, Eric Horstick, and John Carlson for the helpful comments given on earlier manuscript drafts. Flies were kindly shared or acquired from: Shu Kondo, David Krantz, Michael Texada, Jim Truman, Rachel Wilson, Quentin Gaudry, the Blooming-

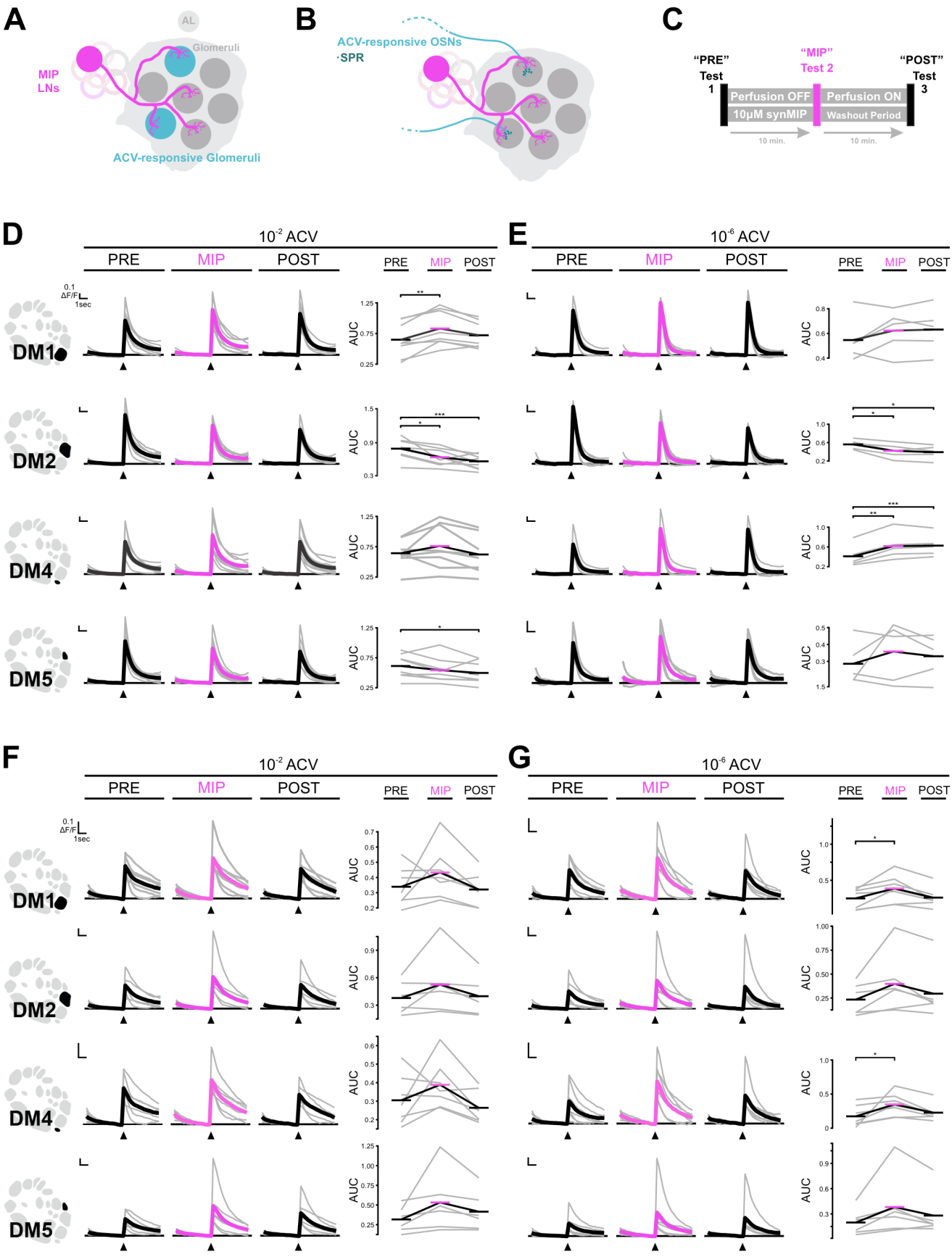

ton Drosophila Stock centers (NIH P40OD018537), and the Janelia Fly Light project for flies. Christian Wegener kindly provided the MIP antibody that was developed by Manfred Eckert. Marco Gallio and Rachel Wil-

Fig. 6. *Previous page.* **MIP differentially effects OSN responses to ACV. (A)** Individual MIPergic LNs (magenta) significantly co-innervate pairs of ACV-responsive glomeruli (cyan). **(B)** ACV-responsive OSNs (cyan) form synaptic connections with MIPergic LNs (magenta) and express the MIP receptor, SPR (turquoise). **(C)** Schematic representation of experimental paradigm for testing MIP's effects on ACV-responsive OSN odor-evoked responses. **(D)** DM1, DM2, DM4, and DM5 OSN responses to 10^{-2} ACV before ("PRE"), after MIP pressure injection ("MIP"), and post-washout ("POST"). MIP significantly increases DM1 OSN responses (p = 0.004, PRE vs. MIP AUC, n = 8; Holm-corrected RM t-tests). Conversely, MIP significantly decreases DM2 and DM5 OSN responses (DM2: p = 0.013, PRE vs. MIP AUC & p = 0.001, PRE vs. POST AUC, n = 8; Holm-corrected RM t-tests; DM5: p = 0.02, PRE vs. POST, n = 8; Holm-corrected RM t-tests). **(E)** DM1, DM2, DM4, and DM5 OSN responses to 10^{-6} ACV as in **(D)**. MIP significantly decreases DM2 OSN responses (p = 0.013, PRE vs. MIP AUC & p = 0.01, PRE vs. POST AUC, n = 5; Holm-corrected RM t-tests). Conversely, MIP significantly increases DM4 OSN responses (p = 0.002, PRE vs. MIP AUC & p = 0.001, PRE vs. POST AUC, n = 5; Holm-corrected RM t-tests). **(F & G)** SPR knockdown in OSNs abolishes MIP-induced decrease in DM2 and DM5 OSN responses (DM2: 10^{-2}: p = 0.136, RM one-way ANOVA, n = 6; 10^{-6}: p = 0.063, PRE vs. MIP AUC & p = 0.688, PRE vs. MIP AUC, n = 6; Holm-adjusted Wilcoxon signed-rank test; DM5: 10^{-2}: p = 0.135, RM one-way ANOVA, n = 6; 10^{-6}: p = 0.063, PRE vs. MIP AUC & p = 0.313, PRE vs. MIP AUC, n = 6; Holm-adjusted Wilcoxon signed-rank test). In contrast, SPR knockdown in OSNs does not abolish MIP-induced increases in DM1 and DM4 OSN responses (DM1: p = 0.031, PRE vs. MIP AUC, n = 7; Holm-adjusted Wilcoxon signed-rank test; DM4: p = 0.031, PRE vs. MIP AUC, n = 7; Holm-adjusted Wilcoxon signed-rank test). For each response: vertical and horizontal scale bars = 0.1 $\triangle$F/F & 1 second (respectively). Glomerular schematics derived from an *in vivo* AL atlas[151].

son graciously provided analysis scripts. Karen Menuz gave helpful insight in the interpretation of RNA-sequencing results from prior work. Stephen Plaza, Alexander Bates, Marta Costa, Greg Jefferis, and Philipp Schlegel gave helpful advice and instruction regarding connectomic analyses, and graciously shared odor scene and valence information. Our connectomic analyses also benefited from discussions in the nat-user community (https://groups.google.com/g/nat-user), and a workshop organized by the Virtual Fly Brain and Drosophila connectomics teams (virtualflybrain.org; WT 208379/Z/17/Z). Fengqiu Diao gave technical advice for creating the SPR^{MI13885}-T2A-LexA::QFAD Trojan exon transgenic animals. Kristyn Lizbinski and James Jeanne graciously provided advice and equipment specifications that lead to the construction and use of the olfactometer system described here. Kristyn Lizbinski, James Jeanne, Marco Gallio, Mehmet Keles, and Gaby Maimon provided invaluable technical advice for performing *in vivo* physiology. Kevin Daly kindly loaned equipment to us for our purposes and gave invaluable technical advice regarding their use. This work was supported by a Grant-In-Aid of Research (G20141015669888) from Sigma Xi, The Scientific Research Society (T.R.S.), start-up funds from WVU (A.M.D.), a National Institutes of Health R03 DC013997 (A.M.D.), a National Institutes of Health R01 DC016293 (A.M.D.), and two AFOSR DURIP awards (FA9550-19-1-0179 and FA9550-20-1-0098) (A.M.D.).

AUTHOR CONTRIBUTIONS

T.R.S. conceived and implemented all experiments, analyzed the subsequent data, prepared figures, and wrote and edited the manuscript. J.J. acquired data that contributed to Figure 3C. A.M.D. acquired funding and helped with manuscript edits.

DECLARATION OF INTERESTS

The authors declare no competing interests.

REFERENCES

1. Nassel, D., Pauls, D., and Huetteroth, W. (2019). Neuropeptides in modulation of Drosophila behavior: how to get a grip on their pleiotropic actions. Curr. Opin. Insect Sci. *36*, 1–8.

2. Jékely, G. (2013). Global view of the evolution and diversity of metazoan neuropeptide signaling. Proc. Natl. Acad. Sci. U. S. A. *110*, 8702–8707.

3. Semmelhack, J.L., and Wang, J.W. (2009). Select Drosophila glomeruli mediate innate olfactory attraction and aversion. Nature *459*, 218–223.

4. Min, S., Chae, H.S., Jang, Y.H., Choi, S., Lee, S., Jeong, Y.T., Jones, W.D., Moon, S.J., Kim, Y.J., and Chung, J. (2016). Identification of a peptidergic pathway critical to satiety responses in drosophila. Curr. Biol. *26*, 814–820.

5. Taghert, P.H., and Nitabach, M.N. (2012). Peptide Neuromodulation in Invertebrate Model Systems. Neuron *76*, 82–97.

6. Katsukura, Y., Ando, H., David, C.N., Grimmelikhuijzen, C.J.P., and Sugiyama, T. (2004). Control of planula migration by LWamide and RFamide neuropeptides in Hydractinia echinata. J. Exp. Biol. *207*, 1803–1810.

7. Golubovic, A., Kuhn, A., Williamson, M., Kalbacher, H., Holstein, T.W., Grimmelikhuijzen, C.J.P., and Gründer, S. (2007). A peptide-gated ion channel from the freshwater polyp Hydra. J. Biol. Chem. *282*, 35098–35103.

8. Kass-Simon, G., and Pierobon, P. (2007). Cnidarian chemical neurotransmission, an updated overview. Comp. Biochem. Physiol. - A Mol. Integr. Physiol. *146*, 9–25.

9. Watanabe, H., Fujisawa, T., and Holstein, T.W. (2009). Cnidarians and the evolutionary origin of the nervous system. Dev. Growth Differ. *51*, 167–183.

10. Conzelmann, M., Offenburger, S.L., Asadulina, A., Keller, T., Münch, T.A., and Jékely, G. (2011). Neuropeptides regulate swimming depth of Platynereis larvae. Proc. Natl. Acad. Sci. U. S. A. *108*.

11. Zieger, E., Robert, N.S.M., Calcino, A., and Wanninger, A. (2021). Ancestral Role of Ecdysis-Related Neuropeptides in Animal Life Cycle Transitions. Curr. Biol. *31*, 1–7.

12. Moroz, L.L., Romanova, D.Y., and Kohn, A.B. (2021). Neural versus alternative integrative systems: Molecular insights into origins of neurotransmitters. Philos. Trans. R. Soc. B Biol. Sci. *376*.

13. Katz, P.S., and Lillvis, J.L. (2014). Reconciling the deep homology of neuromodulation with the evolution of behav-

ior. Curr. Opin. Neurobiol. *29*, 39–47.

14. De Bono, M., and Bargmann, C.I. (1998). Natural variation in a neuropeptide Y receptor homolog modifies social behavior and food response in C. elegans. Cell *94*, 679–689.

15. Inui, A. (1999). Feeding and body-weight regulation by hypothalamic neuropeptides - Mediation of the actions of leptin. Trends Neurosci. *22*, 62–67.

16. Wu, Q., Zhao, Z., and Shen, P. (2005). Regulation of aversion to noxious food by Drosophila neuropeptide Y- and insulin-like systems. Nat. Neurosci. *8*, 1350–1355.

17. Jing, J., Vilim, F.S., Horn, C.C., Alexeeva, V., Hatcher, N.G., Sasaki, K., Yashina, I., Zhurov, Y., Kupfermann, I., Sweedler, J. V., et al. (2007). From hunger to satiety: Reconfiguration of a feeding network by Aplysia neuropeptide Y. J. Neurosci. *27*, 3490–3502.

18. van den Pol, A.N. (2012). Neuropeptide Transmission in Brain Circuits. Neuron *76*, 98–115.

19. Maeda, T., Nakamura, Y., Shiotani, H., Hojo, M.K., Yoshii, T., Ida, T., Sato, T., Yoshida, M., Miyazato, M., Kojima, M., et al. (2015). Suppressive effects of dRYamides on feeding behavior of the blowfly, Phormia regina. Zool. Lett. *1*, 1–10.

20. Ohno, H., Yoshida, M., Sato, T., Kato, J., Miyazato, M., Kojima, M., Ida, T., and Iino, Y. (2017). Luqin-like RYamide peptides regulate food-evoked responses in C. Elegans. Elife *6*, 1–23.

21. Duvall, L.B., Ramos-Espiritu, L., Barsoum, K.E., Glickman, J.F., and Vosshall, L.B. (2019). Small-Molecule Agonists of Ae. aegypti Neuropeptide Y Receptor Block Mosquito Biting. Cell *176*, 687-701.e5.

22. Nässel, D.R., and Zandawala, M. (2019). Recent advances in neuropeptide signaling in Drosophila, from genes to physiology and behavior. Prog. Neurobiol. *179*, 101607.

23. Baraban, S.C., and Tallent, M.K. (2004). Interneuron Diversity series: Interneuronal neuropeptides - Endogenous regulators of neuronal excitability. Trends Neurosci. *27*, 135–142.

24. Carlsson, M. a., Diesner, M., Schachtner, J., and Nässel, D.R. (2010). Multiple neuropeptides in the Drosophila antennal lobe suggest complex modulatory circuits. J. Comp. Neurol. *518*, 3359–3380.

25. Wilson, R.I., and Laurent, G. (2005). Role of GABAergic inhibition in shaping odor-evoked spatiotemporal patterns in the Drosophila antennal lobe. J. Neurosci. *25*, 9069–9079.

26. Schlegel, P., Bates, A.S., Stürner, T., Jagannathan, S.R., Drummond, N., Hsu, J., Capdevila, L.S., Javier, A., Marin, E.C., Barth-Maron, A., et al. (2021). Information flow, cell types and stereotypy in a full olfactory connectome. Elife.

27. Olsen, S.R., Bhandawat, V., and Wilson, R.I. (2007). Excitatory Interactions between Olfactory Processing Channels in the Drosophila Antennal Lobe. Neuron *54*, 89–103.

28. Root, C.M., Masuyama, K., Green, D.S., Enell, L.E., Nässel, D.R., Lee, C.H., and Wang, J.W. (2008). A Presynaptic Gain Control Mechanism Fine-Tunes Olfactory Behavior. Neuron *59*, 311–321.

29. Ignell, R., Root, C.M., Birse, R.T., Wang, J.W., Nässel, D.R., and Winther, A.M.E. (2009). Presynaptic peptidergic modulation of olfactory receptor neurons in Drosophila. Proc. Natl. Acad. Sci. U. S. A. *106*, 13070–13075.

30. Okada, R., Awasaki, T., and Ito, K. (2009). Gamma-aminobutyric acid (GABA)-mediated neural connections in the Drosophila antennal lobe. J. Comp. Neurol. *514*, 74–91.

31. Chou, Y.-H., Spletter, M.L., Yaksi, E., Leong, J.C.S., Wilson, R.I., and Luo, L. (2010). Diversity and wiring variability of olfactory local interneurons in the Drosophila antennal lobe. Nat. Neurosci. *13*, 439–449.

32. Yaksi, E., and Wilson, R.I. (2010). Electrical Coupling between Olfactory Glomeruli. Neuron *67*, 1034–1047.

33. Seki, Y., Rybak, J., Wicher, D., Sachse, S., and Hansson, B.S. (2010). Physiological and morphological characterization of local interneurons in the Drosophila antennal lobe. J. Neurophysiol. *104*, 1007–1019.

34. Das, A., Chiang, A., Davla, S., Priya, R., Reichert, H., VijayRaghavan, K., and Rodrigues, V. (2011). Identification and analysis of a glutamatergic local interneuron lineage in the adult Drosophila olfactory system. Neural Syst. Circuits *1*, 4.

35. Tanaka, N.K., Endo, K., and Ito, K. (2012). Organization of antennal lobe-associated neurons in adult Drosophila melanogaster brain. J. Comp. Neurol. *520*, 4067–4130.

36. Shang, Y., Claridge-Chang, A., Sjulson, L., Pypaert, M., and Miesenböck, G. (2007). Excitatory Local Circuits and Their Implications for Olfactory Processing in the Fly Antennal Lobe. Cell *128*, 601–612.

37. Huang, J., Zhang, W., Qiao, W., Hu, A., and Wang, Z. (2010). Functional connectivity and selective odor responses of excitatory local interneurons in drosophila antennal lobe. Neuron *67*, 1021–1033.

38. Diao, F., Ironfield, H., Luan, H., Diao, F., Shropshire, W.C., Ewer, J., Marr, E., Potter, C.J., Landgraf, M., and White, B.H. (2015). Plug-and-Play Genetic Access to Drosophila Cell Types using Exchangeable Exon Cassettes. Cell Rep. *10*, 1410–1421.

39. Menuz, K., Larter, N.K., Park, J., and Carlson, J.R. (2014). An RNA-Seq Screen of the Drosophila Antenna Identifies a Transporter Necessary for Ammonia Detection. PLoS Genet. *10*.

40. Mohapatra, P., and Menuz, K. (2019). Molecular profiling of the Drosophila antenna reveals conserved genes underlying olfaction in insects. G3 Genes, Genomes, Genet. *9*, 3753–3771.

41. McLaughlin, C.N., Brbić, M., Xie, Q., Li, T., Horns, F., Kolluru, S.S., Kebschull, J.M., Vacek, D., Xie, A., Li, J., et al. (2021). Single-cell transcriptomes of developing and adult olfactory receptor neurons in drosophila. Elife *10*, 1–37.

42. Gupta, A., Wang, Y., and Markram, H. (2000). Organizing principles for a diversity of GABAergic interneurons and synapses in the neocortex. Science (80-.). *287*, 273–278.

43. Markram, H., Toledo-Rodriguez, M., Wang, Y., Gupta, A., Silberberg, G., and Wu, C. (2004). Interneurons of the neocortical inhibitory system. Nat. Rev. Neurosci. *5*, 793–807.

44. Jenett, A., Rubin, G., Ngo, T., Shepherd, D., Murphy,

Dionne, H., Pfeiffer, B., Cavallaro, A., Hall, D., Jeter, J., et al. (2012). A GAL4-Driver Line Resource for Drosophila Neurobiology. Cell Rep. *2*, 991–1001.

45. Nern, A., Pfeiffer, B.D., and Rubin, G.M. (2015). Optimized tools for multicolor stochastic labeling reveal diverse stereotyped cell arrangements in the fly visual system. Proc. Natl. Acad. Sci. U. S. A. *112*, E2967–E2976.

46. Gallio, M., Ofstad, T.A., Macpherson, L.J., Wang, J.W., and Zuker, C.S. (2011). The coding of temperature in the Drosophila brain. Cell *144*, 614–624.

47. Frank, D.D., Enjin, A., Jouandet, G.C., Zaharieva, E.E., Para, A., Stensmyr, M.C., and Gallio, M. (2017). Early Integration of Temperature and Humidity Stimuli in the Drosophila Brain. Curr. Biol. *27*, 2381-2388.e4.

48. Marin, E.C., Büld, L., Theiss, M., Sarkissian, T., Roberts, R.J.V., Turnbull, R., Tamimi, I.F.M., Pleijzier, M.W., Laursen, W.J., Drummond, N., et al. (2020). Connectomics Analysis Reveals First-, Second-, and Third-Order Thermosensory and Hygrosensory Neurons in the Adult Drosophila Brain. Curr. Biol. *30*, 3167-3182.e4.

49. Hallem, E.A., and Carlson, J.R. (2006). Coding of Odors by a Receptor Repertoire. Cell *125*, 143–160.

50. Silbering, A.F., Okada, R., Ito, K., and Galizia, C.G. (2008). Olfactory information processing in the Drosophila antennal lobe: anything goes? J. Neurosci. *28*, 13075–13087.

51. Haddad, R., Weiss, T., Khan, R., Nadler, B., Mandairon, N., Bensafi, M., Schneidman, E., and Sobel, N. (2010). Global features of neural activity in the olfactory system form a parallel code that predicts olfactory behavior and perception. J. Neurosci. *30*, 9017–9026.

52. Nicolaï, L.J.J., Ramaekers, A., Raemaekers, T., Drozdzecki, A., Mauss, A.S., Yan, J., Landgraf, M., Annaert, W., and Hassan, B. a (2010). Genetically encoded dendritic marker sheds light on neuronal connectivity in Drosophila. Proc. Natl. Acad. Sci. U. S. A. *107*, 20553–20558.

53. Zhang, Y.Q., Rodesch, C.K., and Broadie, K. (2002). Living synaptic vesicle marker: Synaptotagmin-GFP. Genesis *34*, 142–145.

54. Schlegel, P., Costa, M., and Jefferis, G.S.X.E. (2017). Learning from connectomics on the fly. Curr. Opin. Insect Sci. *24*, 96–105.

55. Meinertzhagen, I.A. (2018). Of what use is connectomics? A personal perspective on the Drosophila connectome. J. Exp. Biol. *221*.

56. Clements, J., Dolafi, T., Umayam, L., Neubarth, N., Berg, S., Scheffer, L., and Plaza, S. (2020). neuPrint: Analysis Tools for EM Connectomics. bioRxiv, 1–20.

57. Scheffer, L., Xu, C.S., Januszewski, M., Lu, Z., Takemura, S., Hayworth, K., Huang, G., Shinomiya, K., Maitin-Shepard, J., Berg, S., et al. (2020). A connectome and analysis of the adult drosophila central brain. Elife, 1–83.

58. Prokop, A., and Meinertzhagen, I.A. (2006). Development and structure of synaptic contacts in Drosophila. Semin. Cell Dev. Biol. *17*, 20–30.

59. Merighi, A. (2018). Costorage of high molecular weight neurotransmitters in large dense core vesicles of mammalian neurons. Front. Cell. Neurosci. *12*, 1–7.

60. Flanagan, D., and Mercer, A.R. (1989). Morphology and response characteristics of neurones in the deutocerebrum of the brain in the honeybee Apis mellifera. J. Comp. Physiol. A *164*, 483–494.

61. Fonta, C., Sun, X.J., and Masson, C. (1993). Morphology and spatial distribution of bee antennal lobe interneurones responsive to odours. Chem. Senses *18*, 101–119.

62. Sachse, S., and Galizia, C.G. (2002). Role of inhibition for temporal and spatial odor representation in olfactory output neurons: A calcium imaging study. J. Neurophysiol. *87*, 1106–1117.

63. Galizia, C.G., and Kimmerle, B. (2004). Physiological and morphological characterization of honeybee olfactory neurons combining electrophysiology, calcium imaging and confocal microscopy. J. Comp. Physiol. A Neuroethol. Sensory, Neural, Behav. Physiol. *190*, 21–38.

64. Schneider-Mizell, C.M., Gerhard, S., Longair, M., Kazimiers, T., Li, F., Zwart, M.F., Champion, A., Midgley, F.M., Fetter, R.D., Saalfeld, S., et al. (2016). Quantitative neuroanatomy for connectomics in Drosophila. Elife *5*, 1–36.

65. Ding, H., Smith, R.G., Poleg-Polsky, A., Diamond, J.S., and Briggman, K.L. (2016). Species-specific wiring for direction selectivity in the mammalian retina. Nature *535*, 105–110.

66. Frechter, S., Bates, A.S., Tootoonian, S., Dolan, M.J., Manton, J., Jamasb, A.R., Kohl, J., Bock, D., and Jefferis, G. (2019). Functional and anatomical specificity in a higher olfactory centre. Elife *8*, 1–39.

67. Barnes, C.L., Bonnéry, D., and Cardona, A. (2022). Synaptic counts approximate synaptic contact area in Drosophila. PLoS One *17*, e0266064.

68. Lyu, C., Abbott, L.F., and Maimon, G. (2022). Building an allocentric travelling direction signal via vector computation. Nature *601*, 92–97.

69. Holler, S., Köstinger, G., Martin, K.A.C., Schuhknecht, G.F.P., and Stratford, K.J. (2021). Structure and function of a neocortical synapse. Nature *591*, 111–116.

70. Liu, T.X., Davoudian, P.A., Lizbinski, K.M., and Jeanne, J.M. (2022). Connectomic features underlying diverse synaptic connection strengths and subcellular computation. Curr. Biol. *32*, 559-569.e5.

71. Knaden, M., Strutz, A., Ahsan, J., Sachse, S., and Hansson, B.S. (2012). Spatial Representation of Odorant Valence in an Insect Brain. Cell Rep. *1*, 392–399.

72. Yapici, N., Zimmer, M., and Domingos, A.I. (2014). Cellular and molecular basis of decision-making. EMBO Rep. *10*, 1023–1035.

73. Yang, C. hui, Rumpf, S., Xiang, Y., Gordon, M.D., Song, W., Jan, L.Y., and Jan, Y.N. (2009). Control of the Postmating Behavioral Switch in Drosophila Females by Internal Sensory Neurons. Neuron *61*, 519–526.

74. Kim, Y.-J.Y.-C., Bartalska, K., Audsley, N., Yamanaka, N., Yapici, N., Lee, J.-Y., Markovic, M., Isaac, E., Tanaka, Y., and Dickson, B.J. (2010). MIPs are ancestral ligands for the sex peptide receptor. Proc. Natl. Acad. Sci. *107*, 6520–5.

75. Poels, J., Van Loy, T., Vandersmissen, H.P., Van Hiel, B., Van Soest, S., Nachman, R.J., and Van Den Broeck, J.

(2010). Myoinhibiting peptides are the ancestral ligands of the promiscuous Drosophila sex peptide receptor. Cell. Mol. Life Sci. *67*, 3511–3522.

76. Katow, H., Takahashi, T., Saito, K., and Tanimoto, H. (2019). Tango knock-ins visualize endogenous activity of G protein-coupled receptors in Drosophila Tango knock-ins visualize endogenous activity of G protein-coupled receptors. J. Neurogenet. *0*, 1–8.

77. Joseph, R.M., and Carlson, J.R. (2015). Drosophila Chemoreceptors: A Molecular Interface Between the Chemical World and the Brain. Trends Genet. *31*, 683–695.

78. Schmidt, H.R., and Benton, R. (2020). Molecular mechanisms of olfactory detection in insects: Beyond receptors: Insect olfactory detection mechanisms. Open Biol. *10*.

79. Hartenstein, V. (2011). Morphological Diversity and Development of Glia in Drosophila. Glia *59*, 1237–1252.

80. Freeman, M.R. (2015). Drosophila Central Nervous System Glia. Cold Spring Harb. Perspect. Biol. *7*, a020552.

81. Kremer, M.C., Jung, C., Batelli, S., Rubin, G.M., and Gaul, U. (2017). The Glia of the Adult Drosophila Nervous System. Glia *65*, 606–638.

82. Ameku, T., Yoshinari, Y., Texada, M.J., Kondo, S., Amezawa, K., Yoshizaki, G., Shimada-Niwa, Y., and Niwa, R. (2018). Midgut-derived neuropeptide F controls germline stem cell proliferation in a mating-dependent manner. PLOS Biol. *16*, e2005004.

83. Li, H., Horns, F., Wu, B., Luginbuhl, D.J., Quake, S.R., Li, H., Horns, F., Wu, B., Xie, Q., Li, J., et al. (2017). Classifying Drosophila Olfactory Projection Neuron Resource Classifying Drosophila Olfactory Projection Neuron Subtypes by Single-Cell RNA Sequencing. Cell *171*, 1206-1207.e22.

84. Croset, V., Treiber, C.D., and Waddell, S. (2018). Cellular diversity in the Drosophila midbrain revealed by single-cell transcriptomics. Elife *7*, 1–31.

85. Davie, K., Janssens, J., Koldere, D., De Waegeneer, M., Pech, U., Kreft, Ł., Aibar, S., Makhzami, S., Christiaens, V., Bravo González-Blas, C., et al. (2018). A Single-Cell Transcriptome Atlas of the Aging Drosophila Brain. Cell, 982–998.

86. Bell, J.S., and Wilson, R.I. (2016). Behavior Reveals Selective Summation and Max Pooling among Olfactory Processing Channels. Neuron *91*, 425–438.

87. Su, C.Y., Menuz, K., and Carlson, J.R. (2009). Olfactory Perception: Receptors, Cells, and Circuits. Cell *139*, 45–59.

88. Fişek, M., and Wilson, R.I. (2014). Stereotyped connectivity and computations in higher-order olfactory neurons. Nat. Neurosci. *17*, 280–8.

89. Jeanne, J.M., Fisek, M., and Wilson, R.I. (2018). The Organization of Projections from Olfactory Glomeruli onto Higher-Order Neurons. Neuron *96*, 1198–1213.

90. Zhu, H., Hummel, T., Clemens, J.C., Berdnik, D., Zipursky, S.L., and Luo, L. (2006). Dendritic patterning by Dscam and synaptic partner matching in the Drosophila antennal lobe. Nat. Neurosci. *9*, 349–55.

91. Chou, Y., Yang, C., Huang, H., Liou, N., Panganiban, M.R., Luginbuhl, D., Yin, Y., Taisz, I., Liang, L., Jefferis, G.S.X.E., et al. (2022). Mating-driven variability in olfactory local interneuron wiring. Sci. Adv. *7723*, 1–12.

92. Goodman, C.S. (1978). Isogenic grasshoppers: Genetic variability in the morphology of identified neurons. J. Comp. Neurol. *182*, 681–705.

93. Goeritz, M.L., Bowers, M.R., Slepian, B., and Marder, E. (2013). Neuropilar projections of the anterior gastric receptor neuron in the stomatogastric ganglion of the Jonah crab, Cancer borealis. PLoS One *8*, 1–15.

94. Otopalik, A.G., Sutton, A.C., Banghart, M., and Marder, E. (2017). When complex neuronal structures may not matter. Elife *6*, 1–29.

95. Otopalik, A.G., Goeritz, M.L., Sutton, A.C., Brookings, T., Guerini, C., and Marder, E. (2017). Sloppy morphological tuning in identified neurons of the crustacean stomatogastric ganglion. Elife *6*, 1–32.

96. Marder, E., Goeritz, M.L., and Otopalik, A.G. (2015). Robust circuit rhythms in small circuits arise from variable circuit components and mechanisms. Curr. Opin. Neurobiol. *31*, 156–163.

97. Otopalik, A.G., Pipkin, J., and Marder, E. (2019). Neuronal morphologies built for reliable physiology in a rhythmic motor circuit. Elife *8*, 1–24.

98. Thuma, J.B., White, W.E., Hobbs, K.H., and Hooper, S.L. (2009). Pyloric neuron morphology in the stomatogastric ganglion of the lobster, *Panulirus interruptus*. Brain. Behav. Evol. *73*, 26–42.

99. Daur, N., Bryan, A.S., Garcia, V.J., and Bucher, D. (2012). Short-term synaptic plasticity compensates for variability in number of motor neurons at a neuromuscular junction. J. Neurosci. *32*, 16007–16017.

100. Caron, S.J.C., Ruta, V., Abbott, L.F., and Axel, R. (2013). Random convergence of olfactory inputs in the Drosophila mushroom body. Nature *497*, 113–117.

101. Linneweber, G.A., Andriatsilavo, M., Dutta, S.B., Bengochea, M., Hellbruegge, L., Liu, G., Ejsmont, R.K., Straw, A.D., Wernet, M., Hiesinger, P.R., et al. (2020). A neurodevelopmental origin of behavioral individuality in the Drosophila visual system. Science *367*, 1112–1119.

102. Ambros-Ingerson, J., and Holmes, W.R. (2005). Analysis and comparison of morphological reconstructions of hippocampal field CA1 pyramidal cells. Hippocampus *15*, 302–315.

103. Honegger, K., and de Bivort, B. (2018). Stochasticity, individuality and behavior. Curr. Biol. *28*, R8–R12.

104. Honegger, K.S., Smith, M.A.-Y., Churgin, M.A., Turner, G.C., and de Bivort, B.L. (2019). Idiosyncratic neural coding and neuromodulation of olfactory individuality in Drosophila. Proc. Natl. Acad. Sci. *117*, 23292–23297.

105. Rihani, K., and Sachse, S. (2022). Shedding Light on Inter-Individual Variability of Olfactory Circuits in Drosophila. Front. Behav. Neurosci. *16*.

106. Stern, S., Kirst, C., and Bargmann, C.I. (2017). Neuromodulatory Control of Long-Term Behavioral Patterns and Individuality across Development. Cell *171*, 1649-1662.e10.

107. Hussain, A., Üçpunar, H.K., Zhang, M., Loschek, L.F., and Grunwald Kadow, I.C. (2016). Neuropeptides

Modulate Female Chemosensory Processing upon Mating in Drosophila. PLOS Biol. *14*, e1002455.

108. Pantoja, C., Hoagland, A., Carroll, E.C., Karalis, V., Conner, A., and Isacoff, E.Y. (2016). Neuromodulatory Regulation of Behavioral Individuality in Zebrafish. Neuron *91*, 587–601.

109. Liessem, S., Kowatschew, D., Dippel, S., Blanke, A., Korsching, S., Guschlbauer, C., Hooper, S.L., Predel, R., and Büschges, A. (2021). Neuromodulation Can Be Simple: Myoinhibitory Peptide, Contained in Dedicated Regulatory Pathways,Is the Only Neurally-Mediated Peptide Modulator of Stick Insect Leg Muscle. J. Neurosci. *41*, 2911–2929.

110. Smith, S.J., Smbül, U., Graybuck, L.T., Collman, F., Seshamani, S., Gala, R., Gliko, O., Elabbady, L., Miller, J.A., Bakken, T.E., et al. (2019). Single-cell transcriptomic evidence for dense intracortical neuropeptide networks. Elife *8*, 1–35.

111. Sizemore, T.R., and Dacks, A.M. (2016). Serotonergic Modulation Differentially Targets Distinct Network Elements within the Antennal Lobe of Drosophila melanogaster. Sci. Rep. *6*, 37119.

112. Peng, H., Ruan, Z., Long, F., Simpson, J.H., and Myers, E.W. (2010). V3D enables real-time 3D visualization and quantitative analysis of large-scale biological image data sets. Nat. Biotechnol. *28*, 348–353.

113. Erdős, P.L., and Rényi, A. (1961). On a classical problem of probability theory. Mathematics *Ser. A*, 215–220.

114. Wan, Y., Otsuna, H., Holman, H.A., Bagley, B., Ito, M., Lewis, A.K., Colasanto, M., Kardon, G., Ito, K., and Hansen, C. (2017). FluoRender : joint freehand segmentation and visualization for many-channel fluorescence data analysis. BMC Bioinformatics *18*, 1–15.

115. Laissue, P.P., Reiter, C., Hiesinger, P.R., Halter, S., Fischbach, K.F., and Stocker, R.F. (1999). Three-dimensional reconstruction of the antennal lobe in Drosophila melanogaster. J. Comp. Neurol. *405*, 543–552.

116. Couto, A., Alenius, M., and Dickson, B.J. (2005). Molecular , Anatomical , and Functional Organization of the Drosophila Olfactory System. *15*, 1535–1547.

117. Metsalu, T., and Vilo, J. (2015). ClustVis: A web tool for visualizing clustering of multivariate data using Principal Component Analysis and heatmap. Nucleic Acids Res. *43*, W566–W570.

118. Bates, A.S., Schlegel, P., Roberts, R.J.V., Drummond, N., Tamimi, I.F.M., Turnbull, R., Zhao, X., Marin, E.C., Popovici, P.D., Dhawan, S., et al. (2020). Complete Connectomic Reconstruction of Olfactory Projection Neurons in the Fly Brain. Curr. Biol. *30*, 3183-3199.e6.

119. Stensmyr, M.C., Dweck, H.K.M., Farhan, A., Ibba, I., Strutz, A., Mukunda, L., Linz, J., Grabe, V., Steck, K., Lavista-Llanos, S., et al. (2012). A conserved dedicated olfactory circuit for detecting harmful microbes in drosophila. Cell *151*, 1345–1357.

120. Min, S., Ai, M., Shin, S.A., and Suh, G.S.B. (2013). Dedicated olfactory neurons mediating attraction behavior to ammonia and amines in Drosophila. Proc. Natl. Acad. Sci. *110*, E1321–E1329.

121. Ebrahim, S.A.M., Dweck, H.K.M., Stökl, J., Hofferberth, J.E., Trona, F., Weniger, K., Rybak, J., Seki, Y., Stensmyr, M.C., Sachse, S., et al. (2015). Drosophila Avoids Parasitoids by Sensing Their Semiochemicals via a Dedicated Olfactory Circuit. PLoS Biol. *13*, 1–18.

122. Mansourian, S., Corcoran, J., Enjin, A., Löfstedt, C., Dacke, M., and Stensmyr, M.C. (2016). Fecal-Derived Phenol Induces Egg-Laying Aversion in Drosophila. Curr. Biol. *26*, 2762–2769.

123. Vulpe, A., Kim, H.S., Ballou, S., Wu, S.-T., Grabe, V., Nava Gonzales, C., Liang, T., Sachse, S., Jeanne, J.M., Su, C.-Y., et al. (2021). An ammonium transporter is a non-canonical olfactory receptor for ammonia. Curr. Biol., 1–9.

124. Münch, D., and Galizia, C.G. (2016). DoOR 2.0 - Comprehensive Mapping of Drosophila melanogaster Odorant Responses. Sci. Rep. *6*, 1–14.

125. van Breugel, F., Huda, A., and Dickinson, M.H. (2018). Distinct activity-gated pathways mediate attraction and aversion to CO2 in Drosophila. Nature *564*, 420–424.

126. Hong, E.J., and Wilson, R.I. (2015). Simultaneous Encoding of Odors by Channels with Diverse Sensitivity to Inhibition. Neuron *85*, 573–589.

127. Bates, A.S., Manton, J.D., Jagannathan, S.R., Costa, M., Schlegel, P., Rohlfing, T., and Jefferis, G.S.X.E. (2020). The natverse, a versatile toolbox for combining and analysing neuroanatomical data. Elife *9*, 1–35.

128. Coates, K.E., Majot, A.T., Zhang, X., Michael, C.T., Spitzer, S.L., Gaudry, Q., and Dacks, A.M. (2017). Identified Serotonergic Modulatory Neurons Have Heterogeneous Synaptic Connectivity within the Olfactory System of *Drosophila*. J. Neurosci. *37*, 7318–7331.

129. Costa, M., Manton, J.D., Ostrovsky, A.D., Prohaska, S., and Jefferis, G.S.X.E. (2016). NBLAST: Rapid, Sensitive Comparison of Neuronal Structure and Construction of Neuron Family Databases. Neuron *91*, 293–311.

130. Chiang, A.S., Lin, C.Y., Chuang, C.C., Chang, H.M., Hsieh, C.H., Yeh, C.W., Shih, C.T., Wu, J.J., Wang, G.T., Chen, Y.C., et al. (2011). Three-dimensional reconstruction of brain-wide wiring networks in drosophila at single-cell resolution. Curr. Biol. *21*, 1–11.

131. Stocker, R.F., Heimbeck, G., Gendre, N., and de Belle, J.S. (1997). Neuroblast ablation in Drosophila P[GAL4] lines reveals origins of olfactory interneurons. J. Neurobiol. *32*, 443–56.

132. Dacks, A.M., Christensen, T. a., and Hildebrand, J.G. (2006). Phylogeny of a Serotonin-Immunoreactive Neuron in the Primary Olfactory Center of the Insect Brain. J. Comp. Neurol. *498*, 727–746.

133. Tanaka, N.K., Ito, K., and Stopfer, M. (2009). Odor-evoked neural oscillations in Drosophila are mediated by widely branching interneurons. J. Neurosci. *29*, 8595–8603.

134. Sen, S., Biagini, S., Reichert, H., and VijayRaghavan, K. (2014). Orthodenticle is required for the development of olfactory projection neurons and local interneurons in Drosophila. Biol. Open *3*, 711–717.

135. Liu, W.W., and Wilson, R.I. (2013). Glutamate is an inhibitory neurotransmitter in the Drosophila olfactory system.

Proc. Natl. Acad. Sci. *110*, 10294–10299.

136. Lizbinski, K.M., and Dacks, A.M. (2018). Intrinsic and Extrinsic Neuromodulation of Olfactory Processing. Front. Cell. Neurosci. *11*, 1–11.

137. Komiyama, T., Johnson, W.A., Luo, L., and Jefferis, G.S.X.E. (2003). From lineage to wiring specificity: POU domain transcription factors control precise connections of Drosophila olfactory projection neurons. Cell *112*, 157–167.

138. Komiyama, T., and Luo, L. (2007). Intrinsic Control of Precise Dendritic Targeting by an Ensemble of Transcription Factors. Curr. Biol. *17*, 278–285.

139. Weir, P.T., Henze, M.J., Bleul, C., Baumann-Klausener, F., Labhart, T., and Dickinson, M.H. (2016). Anatomical reconstruction and functional imaging reveal an ordered array of skylight polarization detectors in drosophila. J. Neurosci. *36*, 5397–5404.

140. Bhandawat, V., Olsen, S.R., Gouwens, N.W., Schlief, M.L., and Wilson, R.I. (2007). Sensory processing in the Drosophila antennal lobe increases reliability and separability of ensemble odor representations. Nat. Neurosci. *10*, 1474–1482.

141. Dacks, A.M., Christensen, T.A., and Hildebrand, J.G. (2008). Modulation of olfactory information processing in the antennal lobe of Manduca sexta by serotonin. J. Neurophysiol. *99*, 2077–2085.

142. Frank, D.D., Jouandet, G.C., Kearney, P.J., MacPherson, L.J., and Gallio, M. (2015). Temperature representation in the Drosophila brain. Nature *519*, 358–361.

143. Alpert, M.H., Frank, D.D., Kaspi, E., Flourakis, M., Zaharieva, E.E., Allada, R., Para, A., and Gallio, M. (2020). A Circuit Encoding Absolute Cold Temperature in Drosophila. Curr. Biol. *30*, 2275-2288.e5.

144. Ko, K.I., Root, C.M., Lindsay, S.A., Zaninovich, O.A., Shepherd, A.K., Wasserman, S.A., Kim, S.M., and Wang, J.W. (2015). Starvation promotes concerted modulation of appetitive olfactory behavior via parallel neuromodulatory circuits. Elife *4*, 1–17.

145. Oh, Y., Yoon, S.E., Zhang, Q., Chae, H.S., Daubnerová, I., Shafer, O.T., Choe, J., and Kim, Y.J. (2014). A Homeostatic Sleep-Stabilizing Pathway in Drosophila Composed of the Sex Peptide Receptor and Its Ligand, the Myoinhibitory Peptide. PLoS Biol. *12*.

146. Badel, L., Ohta, K., Tsuchimoto, Y., and Kazama, H. (2016). Decoding of Context-Dependent Olfactory Behavior in Drosophila. Neuron *91*, 155–167.

147. Díaz, M.M., Schlichting, M., Abruzzi, K.C., Long, X., and Rosbash, M. (2019). Allatostatin-C/AstC-R2 Is a Novel Pathway to Modulate the Circadian Activity Pattern in Drosophila. Curr. Biol. *29*, 13-22.e3.

148. Zandawala, M., Nguyen, T., Segura, M.B., Johard, H.A.D., Amcoff, M., Wegener, C., Paluzzi, J.P., and Nässel, D.R. (2021). A neuroendocrine pathway modulating osmotic stress in Drosophila.

149. Lin, H.H., Kuang, M.C., Hossain, I., Xuan, Y., Beebe, L., Shepherd, A.K., Rolandi, M., and Wang, J.W. (2022). A nutrient-specific gut hormone arbitrates between courtship and feeding. Nature *602*, 632–638.

150. Fishilevich, E., and Vosshall, L.B. (2005). Genetic and Functional Subdivision of the Drosophila Antennal Lobe Genetic and Functional Subdivision of the Drosophila Antennal Lobe. Curr. Biol. *15*, 1548–1553.

151. Grabe, V., Strutz, A., Baschwitz, A., Hansson, B.S., and Sachse, S. (2015). Digital in vivo 3D atlas of the antennal lobe of Drosophila melanogaster. J. Comp. Neurol. *523*, 530–544.

152. Yew, J.Y., Wang, Y., Barteneva, N., Dikler, S., Kutz-Naber, K.K., Li, L., and Kravitz, E.A. (2009). Analysis of neuropeptide expression and localization in adult Drosophila melanogaster central nervous system by affinity cell-capture mass spectrometry (Journal of Proteome Research (2009) 8, (1271-1284)). J. Proteome Res. *8*, 3786.

153. Root, C.M., Ko, K.I., Jafari, A., and Wang, J.W. (2011). Presynaptic Facilitation by Neuropeptide Signaling Mediates Odor-Driven Food Search. Cell *145*, 133–144.

154. Nojima, T., Rings, A., Allen, A.M., Otto, N., Verschut, T.A., Billeter, J.C., Neville, M.C., and Goodwin, S.F. (2021). A sex-specific switch between visual and olfactory inputs underlies adaptive sex differences in behavior. Curr. Biol. *31*, 1175-1191.e6.

155. Jiang, H., Lkhagva, A., Daubnerová, I., Chae, H.S., Šimo, L., Jung, S.H., Yoon, Y.K., Lee, N.R., Seong, J.Y., Žitňan, D., et al. (2013). Natalisin, a tachykinin-like signaling system, regulates sexual activity and fecundity in insects. Proc. Natl. Acad. Sci. U. S. A. *110*.

156. Grabe, V., Baschwitz, A., Dweck, H.K.M., Lavista-Llanos, S., Hansson, B.S., and Sachse, S. (2016). Elucidating the Neuronal Architecture of Olfactory Glomeruli in the Drosophila Antennal Lobe. Cell Rep. *16*, 3401–3413.

157. Ito, K., Shinomiya, K., Ito, M., Armstrong, J.D., Boyan, G., Hartenstein, V., Harzsch, S., Heisenberg, M., Homberg, U., Jenett, A., et al. (2014). A systematic nomenclature for the insect brain. Neuron *81*, 755–765.

STARMethods

Key Resources Table

REAGENT or RESOURCE	SOURCE	IDENTIFIER
Antibodies		
Rabbit anti-RFP	Rockland	Catalog #: 600-401-379; RRID: AB_2209751
Rabbit anti-DsRed	Clontech	Catalog #: 632496; RRID: AB_10013483
Rat anti-DN-Cadherin	DSHB, University of Iowa	Catalog #: DN-Ex #8; RRID: AB_528121
Rabbit anti-GFP	Thermo Fisher Scientific, CA	Catalog #: A-11122; RRID: AB_221569
Chicken anti-GFP	Abcam	Catalog #: ab13970; RRID: AB_300798
Rabbit anti-Hemagglutinin	Cell Signaling Technology	Catalog #: 3724; RRID: AB_1549585
Mouse anti-V5-Tag::DyLight550	BioRad (formerly AbD Serotec)	Catalog #: MCA1360D550GA; RRID: AB_2687576
Rat anti-FLAG	Novus Bio	Catalog #: NBP1-06712SS; RRID: AB_1625982
Mouse anti-Bruchpilot	DSHB, University of Iowa	Catalog #: nc82; RRID: AB_2314866
Rabbit anti-Myoinhibitory Peptide (MIP)	Manfred Eckert (gift from Christian Wegener)	RRID: AB_2314803
Rat anti-Embryonic lethal abnormal vision (ELAV)	DSHB, University of Iowa	RRID: AB_528218
Mouse anti-Reversed polarity (REPO)	DSHB, University of Iowa	RRID: AB_528448
Goat anti-Rabbit AlexaFluor 488	Thermo Fisher Scientific, CA	Catalog #: A-11008; RRID: AB_143165
Donkey anti-Chicken AlexaFluor 488	Jackson ImmunoResearch Laboratories, Inc.	Catalog #: 703-545-155; RRID: AB_2340375
Donkey anti-Rabbit AlexaFluor 546	Thermo Fisher Scientific, CA	Catalog #: A-10040; RRID: AB_2534016
Goat anti-Mouse AlexaFluor 546	Thermo Fisher Scientific, CA	Catalog #: A-11030; RRID: AB_2534089
Goat anti-Rabbit AlexaFluor 633	Thermo Fisher Scientific, CA	Catalog #: A-21070; RRID: AB_2535731
Goat anti-Mouse AlexaFluor 633	Thermo Fisher Scientific, CA	Catalog #: A-21050; RRID: AB_2535718
Donkey anti-Rat AlexaFluor 647	Abcam	Catalog #: ab150155
Chemicals, peptides, and recombinant proteins		
Odors		
Paraffin oil	J.T. Baker, VWR	CAS #: 8012-95-1
Apple Cider Vinegar (ACV)	Heinz	N/A
2-heptanone	Millipore Sigma	Catalog #: 537683; CAS #: 110-43-0
1-hexanol	Millipore Sigma	Catalog #: H13303; CAS #: 111-27-3
1-octen-3-ol	Millipore Sigma	Catalog # 68225; CAS #: 3391-86-4
Ammonium hydroxide	Millipore Sigma	Catalog #: 221228; CAS #: 1336-21-6
Benzaldehyde	Millipore Sigma	Catalog #: 8.01756; CAS #: 100-52-7
Geranyl acetate	Millipore Sigma	Catalog #: 173495; CAS #: 105-87-3
Synthetic Peptides		
Synthetic MIP (synMIP)	This paper.	N/A
Experimental Models: Organisms/Strains		
w^{*};; $GAD1^{MI09277}$ Trojan LexA::QFAD/TM6B, Tb^{1}	Bloomington Stock Center	RRID: BDSC_60324

w^{*};; $ChAT^{MI04508}$ Trojan LexA::QFAD/TM6B, Tb^{1}	Bloomington Stock Center	RRID: BDSC_60319
w^{*}; VGlut ^{MI04979} Trojan LexA::QFAD/CyO, P{Dfd-GMR-nvYFP}	Bloomington Stock Center	RRID: BDSC_60314
y^{1},w^{*}, 10xUAS-IVS-mCD8::RFP, 13xLexAop-mCD8::GFP	Bloomington Stock Center	RRID: BDSC_32229
w^{-};; GMR32F10-GAL4	Bloomington Stock Center	RRID: BDSC_49725
hs-FlpG5.PEST;; UAS-MCFO-1	Bloomington Stock Center	RRID: BDSC_64085
w^{*}; 10xUAS-IVS-myr::tdTomato	Bloomington Stock Center	RRID: BDSC_32222
w^{*}; 26xLexAop-mCD8::GFP	Bloomington Stock Center	RRID: BDSC_32207
w^{*}; 10xUAS-IVS-mCD8::GFP	Bloomington Stock Center	RRID: BDSC_32185
w^{-}; 20xUAS-IVS-GCaMP6f	Bloomington Stock Center	RRID: BDSC_42747
w^{*}; UAS-SPR-RNAi	Bloomington Stock Center	RRID: BDSC_66888
w^{-}; UAS-DenMark, UAS-syt.eGFP; In(3L)D, $mirr^{SaiD1}$, D^{1}/TM6C, Sb^{1}	Bloomington Stock Center	RRID: BDSC_33064
w^{*};; 13xLexAop-CD4-tdTomato/TM6B, Tb1	Bloomington Stock Center	RRID: BDSC_77139
y^{1},w^{*}, $SPR^{MI13553}$	Bloomington Stock Center	RRID: BDSC_60934
y^{1},w^{*}; wg^{Sp1}/CyO; 13xLexAop2-6xmCherryHA	Bloomington Stock Center	RRID: BDSC_52271
w*,dlg^{14},frt101/FM7a;; $CG11583^{c01124}$,frt80B/TM3, Sb^{1}	Bloomington Stock Center	RRID: BDSC_36283
$SPR^{MI13885}$-T2A-LexA::QFAD	This paper.	N/A
y^{1}, w^{-}, SPR-T2A-GAL4	Shu Kondo, Tohoku University	Katow et al., 2019
Pebbled-GAL4 (Peb-GAL4)	Rachel Wilson, Harvard University	N/A
SPR-GAL4::VP16	Jim Truman, University of Washington (by way of Michael Texada, University of Copenhagen)	Ameku et al., 2018 Flybase ID: FBti0201391
Recombinant DNA		
pBS-KS-attB2-SA(2)-T2A-LexA::QFAD-Hsp70	Daio et al., 2015	Addgene Catalog #62949
Software and Algorithms		
VAA3D (v.3.20)	Peng et al., 2010	RRID: SCR_002609
FluoRender (v.2.26.3)	Wan et al., 2017	RRID: SCR_014303
FIJI (v.2.0.0)	Open-Source	RRID:SCR_002285
R (v.4.1.1)	Open-Source	www.R-project.org
R Studio (v.2021.09.0)	Open-Source	www.rstudio.com
MATLAB 2021a	MathWorks	www.mathworks.com
Python 3	Open-Source	RRID: SCR_008394
CorelDRAW 2021	Corel Corp.	www.corel.com
Adobe Illustrator 2022	Adobe Inc.	www.adobe.com
SCope	Davie et al., 2018	www.scope.aertslab.org
Natverse	Bates et al., 2020; Schlegel et al., 2021	www.natverse.org
Connectome-neuprint/neuprint-python	Stuart Berg (JRC)	N/A
CloudVolume	William Silversmith (Princeton)	www.github.com/seung-lab/cloud-volume
ScanImage (v.5.5)	Vidrio Technologies	N/A

RESOURCE AVAILABILITY

Lead Contact

Further information and reasonable requests for reagents and resources should be directed to and will be fulfilled by the lead contact, Tyler R. Sizemore (sizemoretyler92@gmail.com).

Materials Availability

All novel transgenics generated here will be deposited with the Bloomington Drosophila Stock Center post-publication.

Data and Code Availability

With the exception of code that was graciously provided to us by others, all code that was used to analyze or plot data is available from the lead contact upon reasonable request. Any additional information required to reanalyze the data reported here is available from the lead contact upon reasonable request.

EXPERIMENTAL MODEL AND SUBJECT DETAILS

Flies were reared on standard cornmeal and molasses media at 24°C and under a 12:12 light:dark cycle. Equal numbers of male and female animals were used when possible, excluding live-imaging experiments which used only females. For mating status comparisons: 1) "virgin females" denotes females that were meconium-positive upon collection, 2) non-virgin females were housed with males until processing for immunohistochemistry, and 3) flies were age-matched and kept on the similar media until processed for immunohistochemistry. The genotypes used for each experiment are included in **Supplementary Table 1**.

METHOD DETAILS

A. Immunohistochemistry and Imaging. All immunohistochemistry was performed generally as previously described[111]. Briefly, samples were dissected, fixed in 4% paraformaldehyde, then washed with phosphate buffered saline with 0.5% Triton-X 100 (PBST) several times before taking samples through an ascending-descending ethanol was series, then blocking in 4% IgG-free BSA (Jackson Immunoresearch; Cat#001-000-162). Samples were then incubated in primary antibody (**Key Resources Table**) diluted in blocking solution and 5mM sodium azide. Following primary antibody incubation samples were washed with PBST, blocked, and incubated in secondary antibody diluted in blocking solution and 5mM sodium azide. Finally, samples were washed, cleared using an ascending glycerol series (40%, 60%, 80%), and mounted on well slides in Vectashield (Vector Laboratories, Burlingame, CA; Cat#H-1200). Images were collected and analyzed as previously described[111] with VAA3D[112] and FluoRender[114], apart from those captured with a 40x/1.25 Silicone UPlanSApo Olympus objective.

B. Single LN Clone Induction and Glomerular Innervation Analysis. Single LN clones were induced through the MultiColor Flip Out (MCFO) method[45]. Flies carrying the MCFO cassettes, Flp-recombinase, and GAL4 driver were raised under normal conditions (see above) until heat shock. Adult flies were heat-shocked in a 37°C water bath for 12-25 minutes and returned to normal conditions for ~2-3 days before processing for immunohistochemistry. We chose to analyze the innervation patterns of 50 individual MIPergic LNs based on a statistical probability theorem termed, "the coupon collector problem"[113]. For our purposes, this meant we needed to sample 43 individual LNs to ensure we sampled each of the ~13 LNs highlighted by R32F10-GAL4 **(Figure 1B-1D)**. We chose to analyze more than the minimal number as determined by this theorem as an additional preemptive measure to ensure the ~8 MIPergic AL LNs were sampled. Apart from VA1v, glomeruli were defined according to previously published AL maps[115,116]. Glomerulus names were later updated according to recent naming conventions[26]. Neuropil were labeled using anti-DN-cadherin or anti-Bruchpilot (**Key Resources Table**). Hierarchical clustering and principal components analysis (PCA) of glomerular innervation data were performed as previously described[31]. PCA was performed without any arbitrary threshold of significance. Data were clustered using Ward's method ("ward.D2") and Euclidian distance using the *ClustVis* package (https://github.com/taunometsalu/ClustVis)[117]. Pairwise Pearson's correlation coefficient of MIPergic LN glomerular innervation were determined using the "cor" function in the base-R *stats* package, and significant correlations were subsequently assessed using the "rcorr" function in the *Hmisc* package. The *corrplot* package was used to create the hierarchically clustered (using Ward's method) representation of these pairwise correlation coefficients depicted in **Figure 1**. In every case used, glomerular "odor scene" information is derived from previous assignments[118].
To determine if MIPergic LNs preferentially innervate glomeruli based on valence, glomeruli were assigned "attractive" or "aversive" based on similar assignments previously described[26,118]. These glomerular valences aggregate findings from previ-

ous reports[3,119–123], as well as behavioral valence of the odors[71] that glomerulus' OSNs respond to according to DoOR 2.0[124]. Glomeruli whose valence is state-dependent (i.e., the V glomerulus)[125] and DC4 were not included in this analysis. Similar methods were used to determine if MIPergic LNs preferentially innervate glomeruli based on the functional group of a given OR's cognate odorant, with the exception of the V and VM6 glomeruli.

C. MIPergic LN Anatomical Marker Density Analyses. Analysis of syt.eGFP, DenMark, anti-MIP immunoreactive puncta signal, and LN innervation (via mCD8::GFP signal) density in antennal lobe glomeruli was performed as previously described[126]. Images of all antennal lobes within a given brain were collected with similar confocal scan settings (laser power, detector offset, etc.) and later imported into FIJI for quantification. Using the Segmentation Editor plugin and a previously described script (graciously provided by Rachel Wilson, Harvard)[126], ROIs were manually traced every 2-3 slices around the neuropil boundaries of each glomerulus using the anti-DN-Cadherin or anti-Bruchpilot channel, and then interpolated through the stack to obtain boundaries in adjacent slices. To ensure each brain contributed equally when pooling data across brains, signal density values for all glomeruli were normalized to the maximum density value within the given indicator being analyzed (e.g., all density values for syt.eGFP were normalized to the maximum syt.eGFP value). The "ggscatter" function in the *ggpubr* package was used to determine Pearson's correlation coefficients and p-values when assessing correlations between effector/anti-MIP and MIPergic LN mCD8::GFP voxel density across all glomeruli. Adjusted R-squared values were calculated using the base-R *stats* package and correspond to how well each data being assessed for the given correlation analysis fit a linear model.

D. Putative MIPergic LN Connectomic Analyses - Identifying Putative MIPergic LNs. All connectome analyses leveraged the publicly available Janelia FlyEM *Drosophila* hemibrain electron microscopy volume (v.1.2.1; https://neuprint.janelia.org/)[56,57], and recently described analysis suites[26,127]. We used several criteria for determining which neurons are most likely MIPergic LNs, the first of which was the candidate neurons must be AL LNs. Next, we selected those candidate LNs that receive input from the serotonergic CSD neurons as all MIPergic LNs express the 5-HT1A serotonin receptor[111], and form connections with the serotonergic CSD neurons[128]. We then used *natverse*[127] to transform the interconnectivity of each candidate neuron into the FlyCircuit whole brain (FCWB) template brain three- dimensional space[129,130], so we could generate a morphological similarity score between our query neuron and neurons FlyLight project's GMR-GAL4 repository[44] by using the built-in NBLAST package (*nat.nblast*)[129]. We selected for only those candidates that achieved a GMR32F10-GAL4 NBLAST score of >0.60 ["identical twins"[129]]. Lastly, any remaining candidate MIPergic LNs were filtered for those neurons that are considered "Traced", the hemibrain's highest level of tracing completeness and confidence. Only neurons that met all of these criteria (~10% of all AL LNs) were considered for further analysis.

E. Putative MIPergic LN Connectomic Analyses - putMIP LN Meshes, Segregation Indices, and Flow Centrality. Most methods for analyzing putMIP LN morphology and connectivity have been described recently[26]. Putative MIPergic LN skeleton meshes **(Figure 2F)** were fetched from the hemibrain data repository by accessing the neuPrint Python API using the *neuprint-python* (https://github.com/connectome-neuprint/neuprint-python) and *Cloud-Volume* (https://github.com/seung-lab/cloud-volume) packages. The *hemibrainr* package (https://github.com/flyconnectome/hemibrainr) was used to fetch each putMIP LN's metadata and calculate each neuron's dendrite-axon segregation index and flow centrality[64] using the recommended arguments.

F. Putative MIPergic LN Connectomic Analyses - Intraglomerular Axon:Dendrite Ratio Analysis. Glomerular meshes based on PN dendrites were used for all subsequent analyses (axon:dendrite ratio by glomerulus, connectivity demographics, etc.)[26]. To establish a postsynaptic:presynaptic ratio for each glomerulus a given putMIP LN innervates, we extracted the number of pre- and postsynaptic sites each putMIP LN has within each glomerulus by subsetting the connectors read in by the *neurprintr* "neuprint_read_neurons" function. These connectors were then filtered for their presence inside each glomerulus' mesh XYZ coordinate space, segregated based on whether they were a post- or presynaptic site, then finally summed. We used the following formula to establish a given putMIP LN's axon:dendrite ratio across all glomeruli: *(# of postsynaptic sites - # of presynaptic sites)/(# of postsynaptic sites + # of presynaptic sites)*. Therefore, values from negative one to zero indicate the given putMIP LN has more presynaptic sites within a given glomerulus. Conversely, values from zero to positive one indicates the given putMIP LN has more postsynaptic sites within a glomerulus.

G. Putative MIPergic LN Connectomic Analyses - General Upstream and Downstream Demographics Analyses. To identify and compare the demographics of each putMIP LN's upstream and downstream partners, putMIP LN connectivity data were first extracted using the *hemibrainr* "simple connectivity" function. The demographic of each presynaptic and postsynaptic partner was generally assigned according to the neuron's accompanying "name" or "type" as listed on neuPrint. In cases where a neuron's "name" or "type" was unannotated ("NA"), the neuron would be categorized as "Unknown". We used the following formula to determine the percentage of overall input a given putMIP LN receives from a given neuron category: [(*sum of connections from a given neuron category to the given putMIP LN*)/(*summed amount of input that given putMIP LN*

receives from all categories)] x *100%*. Similar methods were applied for determining the percentage of overall output a given neuron category receives from a given putMIP LN.

H. Putative MIPergic LN Connectomic Analyses - putMIP LN Input Polarity Analysis. To determine the amount of excitatory, inhibitory, and modulatory input a given putMIP LN receives within each glomerulus, we first categorized each presynaptic neuron as either excitatory, inhibitory, or modulatory based on the presynaptic neuron's neuPrint "name"/"type", previous immunochemistry results[30,31,34,131–134], and/or the category assigned in previous reports[26]. However, we acknowledge several caveats to this analysis, such as: (1) this analysis does not account for co-transmission; (2) several glomeruli are truncated within the hemibrain AL[26]; (3) although we consider all LNs as inhibitory as most are either GABAergic or glutamatergic (combined, these represent ~170/200 AL LNs)[30,31,34,131,133,135], there are ~4 tyrosine hydroxylase-immunoreactive (dopaminergic) and ~8-15 cholinergic and/or electrically coupled LNs in the AL[31,32,36,37]; (4) although GABA can also act as an intrinsic modulator in the AL (reviewed by Lizbinski & Dacks[136]), we only count GABAergic LNs as part of the "inhibitory input" category here; and, (5) we consider all ventral LNs analyzed here as being glutamatergic, but there are ~1-2 dopaminergic (tyrosine hydroxylase-immunoreactive) ventral LNs[31]. Once each presynaptic neuron's chemical identity (excitatory, inhibitory, or modulatory) was determined, we used several approaches to assign these synapses to particular glomeruli. In the case of uniglomerular PNs (uPNs) and OSNs, we leveraged the single glomerulus innervation of these presynaptic neuron types to assign their synapse onto a given putMIP LN synapse to the presynaptic neuron's home glomerulus. That is to say, OSN-to-putMIP LN and uPN-to-putMIP LN synapses were assigned to a glomerulus by: (1) using the home glomerulus assigned to a given presynaptic in the neuron's neuPrint "name"/"type", or (2) by the home glomerulus assigned to the neuron in previous reports[26]. For instance, if the presynaptic neuron was a cholinergic PN whose home glomerulus is DA2, and this DA2 PN synapses on a given putMIP LN five times, then those five synapses went to the overall excitatory input the given putMIP LN receives within DA2. Neurons were only excluded from this analysis if the presynaptic neuron's home glomerulus was not previously identified[26]. Once the polarity of the input type was established, we used the same methods as above for determining whether the XYZ coordinates of each putMIP LN's synapse(s) with a given presynaptic partner were located in a given glomerulus. Synapse counts for each putMIP LN partner within the given glomerulus were then summed by type (excitatory, inhibitory, or modulatory), and the resulting total was divided by the total number of synapses the given putMIP LN makes within that glomerulus to establish percent excitatory, inhibitory input, or modulatory input.

I. SPR^{MI13885}-T2A-LexA::QFAD Generation. The SPR^{MI13885}-T2A-LexA::QFAD fly line was established using previously described injections methods[38]. We also note that we also attempted to create an SPR-T2A-GAL4 using the pC-(lox2-attB2-SA-T2A-Gal4-Hsp70)3 construct (Addgene #62957), but no founders emerged (potentially owing to lethality when these construct elements are inserted in the SPR locus). Briefly, pBS-KS-attB2-SA(2)-T2A-LexA::QFAD-Hsp70 and ΦC31 helper plasmid DNA were co-injected into y^1, w^*, Mi{MIC}SPR^{MI13885}. pBS-KS-attB2-SA(2)-T2A-LexA::QFAD-Hsp70 (Addgene plasmid #62949) and pC-(lox2-attB2-SA-T2A-Gal4-Hsp70)3 (Addgene #62957) were gifts from Benjamin H. White (NIH). SPR^{MI13885}-T2A-LexA::QFAD transformants were isolated as depicted in **Figure S7**.

J. Single-Cell RNA-Sequencing (scRNA-seq) Analysis of SPR Expression. Single-cell transcriptomic data were accessed and downloaded from the SCope web interface (https://scope.aertslab.org) on 03/04/2022. Projection neuron clusters were re-identified as in each dataset's original report[83–85]. Transcript reads were exported log-transformed (log(1 + x)) and reads were counts-per-million (CPM) normalized. Projection neuron subpopulations were then identified within each scRNA-seq dataset using previously established marker genes[83,137,138].

K. *in vivo* Calcium Imaging - Animal Preparation. All calcium imaging experiments were performed on female flies ~1-5 days post-eclosion, and at room temperature. Animals of the proper genotype were collected and briefly anesthetized on ice. Once anesthetized, an animal was affixed to a custom-built holder with UV curable glue (BONDIC, M/N: SK8024). Our custom-built holder consists of a sheet of aluminum foil with a ~1x1mm square (the imaging window) affixed to a 3D-printed design derived from similar designs described previously[139]. Once mounted, a small window exposing the dorsal side of the brain was created, and covered with twice-filtered recording saline (in mM: 2 $CaCl_2$, 5 KCl, 5 HEPES, 8.2 $MgCl_2$, 108 NaCl, 4 $NaHCO_3$, 1 NaH_2PO_4, 10 sucrose, and 5 trehalose; adjusted pH: ~7.4)[28]. After establishing the imaging window, the air sacs, fat bodies, and trachea covering the dorsal side of the brain - as well as Muscle 16 - were removed with fine forceps. With the exception of minimal epochs during the synthetic MIP bath application experiments (see below), the brain was continuously perfused with oxygenated (95%O_2/5%CO_2) recording saline using a Cole-Parmer Masterflex C/L (M/N: 77120-62) at a rate of ~2mL/min.

L. *in vivo* Calcium Imaging - Image Acquisition. For one-photon imaging data (the majority of *in vivo* physiology data), data were acquired using a Prior Scientific Open Stand (M/N: H175) microscope mounted on Prior Scientific motorized translational stage (M/N: HZPKT1), and equipped with an Olympus 10x/0.30 UPlanFL N objective and an Olympus 60x/1.00 LUMPlanFL N water-immersion objective. A 470nm CoolLED pE-100 (CoolLED Ltd., Hampshire, UK) was used as the light

source. Each trial was captured with a Hamamatsu ORCA-4.0LT camera (Hamamatsu Phototonics, Hamamatsu, Japan), and consists of 40 1,024x1,024 frames acquired at a frame rate of ~9 Hz.

A portion of the R32F10-GAL4 odor panel experiments were also acquired using a custom-built two-photon system (Scientifica) equipped with a Mai Tai HP Ti:Sapphire laser (Spectra-Physics) and operated using ScanImage acquisition software (v.5.5; Vidrio Technologies). Each two-photon imaging trial was captured by a Scientifica SciCam Pro camera, and consisted of 80 512x512 frames acquired at a frame rate of ~3.4 Hz. After data acquisition, a high-resolution z-stack (1,024x1,024) was acquired at ~0.21 Hz to enable post-hoc glomerulus identification (see below).

M. *in vivo* Calcium Imaging - Odor Preparation and Delivery. All odor concentrations are reported as v/v dilutions in paraffin oil (J.T. Baker, VWR #JTS894), or autoclaved and twice-filtered distilled water (for diluting acids). For example, 10^{-2} dilution indicates that one volume of an odor is diluted with 100 volumes of paraffin oil. For one-photon imaging data (the majority of *in vivo* physiology data), dilutions were prepared in 2mL odor vials (SUPELCO; P/N: 6020) that contained a final volume of 1mL of diluted odor in paraffin oil every other day, or after two experiments (whichever came first). Odors were generally presented as previously described[88,115,129]. Briefly, a carrier stream of carbon-filtered, dehumidified, air was presented at 2.2 L/min to the fly continuously through an 8mm Teflon tube placed ~1cm away from the fly. A three-way solenoid (The Lee Company, P/N: LHDA1231315H) diverted a small portion of the airstream (0.2 L/min) through the headspace of an odor vial for 200ms after triggering an external voltage command (TTL pulse) at frame 20 of the trial. Considering the above, the odor is diluted further (by 10-fold) prior to delivery to the animal. The odor stream joined the carrier stream 11cm from the end of the tube, and the tube opening measured ~4mm. Odor delivery during two-photon imaging was similar, but differed slightly in that: (1) odor cartridges (see below) instead of a 2mL odor vial; (2) the continuous airstream was presented via a custom-built glass tube; and, (3) the TTL pulse occurred at frame 30 of the trial.

Methods for assessing preparation health and performing multiple odor trials generally conform to previous work[89,126]. At the start of each experiment, the animal was presented a test odor (10^{-3} 2-heptanone) to assess the preparation's health. Only the data collected from animals whose responses to this test odor were robust and did not dramatically change from baseline over the course of the experiment were used for further analysis. The only exceptions to this were those data collected in synthetic MIP bath application experiments (see below), since bath application of any modulator would likely result in network property changes that would consequently change olfactory responses. Therefore, the test odor was only initially presented to those animals used for synthetic peptide application experiments, so their initial olfactory response health could be assessed. Each experiment consisted of multiple odor trials (3 for OSNs; 4 for LNs) within a preparation which were then averaged to attain a within-animal response. These within-animal averages were subsequently averaged across many animals for subsequent statistical analysis, and "n" is reported as the number of animals. Each odor trial consisted of five 200ms pulses of odor with a 1ms interpulse interval. The same odor was never presented twice within 2min to prevent depletion of the odor vial's headspace. If multiple odors were to be tested, then they were presented randomly. If multiple concentrations of a given odor were to be tested, then the lower concentration was presented before the higher concentration. Air entered and exited each odor vial through a PEEK one-way check valve (The Lee Company, P/N: TKLA3201112H) connected to the vial by Teflon tubing. The odor delivery tube was flushed with clean air for 2min when changing between odors/concentrations. As an additional preemptive measure, all odor delivery system components were hooked up to the house vacuum line overnight. The olfactometer used in two-photon data collection consisted of odor cartridges (a syringe housing a piece of filter paper that was doused in 10µl of diluted odor) hooked into a custom glass carrier stream delivery tube as previously described[141].

N. *in vivo* Calcium Imaging - Data Analysis. All calcium imaging data were analyzed using a custom-made MATLAB script graciously provided by Marco Gallio (Northwestern University) and has been described previously[47,142,143]. With the exception of any preparations that violated the aforementioned criteria (e.g., movement, diminishing prep health, etc.), no data points or outliers were excluded from our analyses. Generally, the number of flies to be used for experiments are not a limiting factor, therefore no statistical power analyses were used to pre-determine sample sizes. Regardless, our sample sizes are similar to those in previous reports that perform similar experiments[29,47,144–149]. Before analyzing the data, a Gaussian low-pass filter (sigma=1), bleach correction (exponential fit), and image stabilizer algorithms were applied to the given trial's raw ΔF/F signal. Similar preprocessing for two-photon microscopy data was similar, with the exception of a higher sigma during Gaussian low-pass filtering (sigma=2). A trial's average fluorescence image was used as a guide to draw consistently sized circular regions-of-interest (ROI) within a given glomerulus. Calcium transients (ΔF/F) within the ROI were measured as changes in fluorescence (ΔF) normalized to baseline fluorescence (F, fluorescence intensity averaged across 2sec just prior to odor onset). Within-animal responses were established by averaging across several odor trials in the given preparation (3 for OSNs; 4 for LNs). These within-animal responses were then pooled for each stimulus identity and concentration across animals. These pooled averages were used for all subsequent statistical analyses and the "n" is reported as the number of animals. Glomeruli were manually identified post-hoc by comparing acquired images to well-defined three-dimensional maps of the AL[150,151]. Only the glomeruli that were reasonably identifiable were considered for analysis.

O. Synthetic Myoinhibitory Peptide (synMIP) Application Experiments. Synthetic MIP (synMIP; EPTWNNLKGMW-amide) was custom made by GenScript (Piscataway, NJ, USA) at the highest purity available (>75%). The sequence we chose to use for synMIP is identical to the sequence previous investigations have used when discerning the role of MIP in the *Drosophila* circadian system[145]. In pilot experiments, we tested another sequence of synthetic MIP (RQAQGWNKFRGAW-amide) that was previously detected at the highest abundance by direct profiling of single ALs using mass spectrometry[24,152]. Experimental results produced using synthetic peptide of either sequence were not qualitatively different, but all results reported here use the synMIP previously used in circadian studies[145]. To test how synMIP application adjusts odor-evoked responses, a 1,000μM working solution was made by diluting a small portion of the lyophilized peptide in nuclease-free water (Thermo Scientific, #R0581). After testing the initial odor-evoked responses of the neurons being tested for a given experiment, the perfusion system was switched off momentarily so a small portion of our synMIP working solution could be pressure injected into the AL to a final concentration of 10μM. This final concentration was chosen so as to be comparable to similar studies[144,153]. Ten minutes after synMIP pressure injection, the animal's odor-evoked responses were tested as before synMIP injection, and then the perfusion system was switched back on. Ten minutes after turning the perfusion system back on, the animal's odor-evoked responses were once again tested as they were initially. Re-testing the animal's response to the test odor (10^{-3} 2-heptanone) at the end of these experiments could not be used as a reliable means for assessing prep health due to changes in circuit member responses induced by modulator bath application. Therefore, for these experiments no animal was tested for longer than the average time that animals were reliably healthy in the MIPergic LN odor panel experiments (~90min). Furthermore, we believe these preparations remain healthy throughout the entire experimental epoch as ACV responses increase or do not significantly diminish over the course of the experimental epoch in many glomeruli **(Figure 6)**.

QUANTIFICATION AND STATISTICAL ANALYSES

P. Quantification and Statistical Analyses - General Approach. Statistical analyses were performed using R (v.4.1.1) in R Studio (v.2021.09.0). Values to be analyzed were concatenated in Excel before importing into the relevant analysis software. Statistical results are reported where applicable and summarized in **Supplementary Table 1**. All statistical tests were two-tailed. All boxplots display the minimum, 25th-percentile, median, 75th-percentile, and maximum of the given data. Additional analysis details are provided for each set of experiments above. Where possible, values are given as mean±SEM. Statistical significance is defined as: *p 0.05, **p 0.01, ***p 0.001.

Q. Quantification and Statistical Analyses - Anatomical Analyses. The *ClustVis* package was used to hierarchically cluster (using Ward's criteria) and perform PCA on individual MIPergic LN innervation patterns. The "cor" function in the base-R *stats* package and the "rcorr" function in the *Hmisc* package were used to calculate statistically significant Pearson's correlation coefficients for MIPergic LN pairwise glomerular innervation patterns. The *ggpubr* package's "ggscatter" function was used to determine Pearson's correlation coefficients and p-values when assessing correlations between: (1) effector/anti-MIP and MIPergic LN mCD8::GFP voxel density across all glomeruli, and (2) MIPergic LN glomerular innervation frequency as a function of each glomerulus' volume. Adjusted R-squared values were calculated using the base-R *stats* package and correspond to how well each data being assessed for the given correlation analysis fit a linear model. The Shapiro-Wilk test (the *rstatix* package's "shapiro_test" function) was used to evaluate any deviations from a normal distribution. Welch's unpaired t-test was used to determine if MIPergic LNs preferentially innervate glomeruli based on inferred hedonic valence. A Kruskal-Wallis rank sum test followed by pairwise Bonferroni's-corrected Dunn's multiple comparisons test of was used to determine if: (1) MIPergic LNs preferentially innervate based on the functional group found along the odorant that activates the given glomerulus' OR; (2) SPR-GAL4::VP16 expression in antennae and maxillary palps significantly differs between males, mated females, and virgin females; (3) SPR-GAL4::VP16 expression in glutamatergic LNs between males, mated females, and virgin females; (4) SPR-T2A-GAL4 expression in maxillary palps significantly differs between males, mated females, and virgin females; and, (5) the number of MIPergic LNs differ between males, mated females, and virgin females. Welch's one-way ANOVA with a Bonferroni multiple comparisons correction was used to assess statistically significant differences in SPR-T2A-GAL4 expression in antennae between males, mated females, and virgin females. To resolve any sexual dimorphism in MIPergic LN syt.eGFP or DenMark puncta density across glomeruli, we used a two-way ANOVA with a Greenhouse-Geisser sphericity correction followed by a Bonferroni's multiple comparisons test.

R. Quantification and Statistical Analyses - *in vivo* Calcium Imaging. Background-subtracted changes in fluorescence over time (ΔF/F) analyses were carried out using custom MATLAB scripts previously described[47,142], and are represented as individual traces overlaid by the mean with dilutant-only (e.g., paraffin oil-only) responses subtracted. Average peak response **(Figure 3E)** refers to the maximal ΔF/F value within the time of odor onset to ~1 second post-odor onset averaged across all animals. Area under the ΔF/F curve (AUC) was modified from previous reports[154], such that AUC was calculated using Simpson's rule ("sintegral" function in *Bolstad2* package) as the integral of the ΔF/F traces from the beginning until 1 second

after odor delivery with a baseline of 1 second before stimulus onset. To assess OSN odor-evoked response (AUC) differences across synMIP treatments, we first determined if normality could be assumed (as above). If normality could be assumed, then an omnibus repeated measures one-way ANOVA with a Greenhouse-Geisser sphericity correction was performed (RM one-way ANOVA) ("anova_test" function in *rstatix*). If significant differences were detected with the omnibus, then pairwise repeated measures t-tests (RM t-tests) with a Holm multiple comparisons correction were performed to identify which groups were statistically different. If normality could not be assumed, then a Friedman rank sum test followed by Holm-corrected paired two-sided Wilcoxon signed-rank test was performed.

SUPPLEMENTAL INFORMATION

Figure Legends.

Figure S1 Myoinhibitory peptide (MIP) colabeling with transgenic markers for GABAergic, cholinergic, and glutamatergic neurons in the *Drosophila* central brain. **(A)** Regardless of sex or mating status, there are no MIP-immunoreactive (MIP-ir) OSNs in *Drosophila*. The left most diagram represents the imaging plane for all images to the right, wherein: **1-1"** = OSNs in the 3rd-antennal segment; **2-2"** = maxillary palp OSNs. High-contrast black-and-white images for each individual label (ChAT Trojan LexA-derived tdTomato or anti-MIP) are shown below each merged image (images in color). **(B)** MIPergic neurons in the antennal lobe (AL) **(Figure 1)** and near the median bundle (MBDL) colabel with glutamic acid decarboxylase 1 (GAD1). MIPergic neurons in the superior medial and lateral protocerebrum (SMP and SLP, respectively) and near the lateral medial lobula (LMlo) colabel with vesicular glutamate transporter (VGlut). MIPergic neurons within the inferior contralateral interneuron cluster (ICLI)[155] and SEZ do not colabel for ChAT, GAD1, or VGlut, and are most likely tyraminergic (Tyr) based on scRNA-seq data[84]. **(C)** Schematic summarizing data from **(A)**, wherein several populations of MIP-immunoreactive neurons are also glutamatergic (MIP^+ & $VGlut^+$ neurons in the SMP, LMlo, and SLP; magenta), two populations are also GABAergic (MIP^+ & $GAD1^+$ neurons in the MBDL and AL) **(see also Figure 1)**, and no MIP-immunoreactive neurons are cholinergic (colabel with ChAT). Except for the ICLI interneurons, soma locations are labeled according to the closest neuropil, or fascicle, according to established nomenclature[157]. **(D)** The number of MIP-ir AL LNs does not differ based on sex or mating status ($p = 0.548$, Kruskal-Wallis rank sum test). Cell counts: n = 12 brains, 24 ALs (mated female); n = 16 brains, 31 ALs (virgin female) ; n = 7 brains, 14 ALs (male). In all cases: neuropil was delineated by anti-DN-cadherin staining; open arrowheads = no colocalization; closed arrowheads = colocalization.

Figure S2 MIPergic LNs do not preferentially innervate olfactory glomeruli based on odor-evoked behavioral valence, the odor-tuning properties of a given glomeruli's olfactory receptor neuron(s), or the size of the glomerulus. **(A)** Dot plot representation of the frequency we find a given glomerulus is innervated by a single MIPergic LN clone. Rectangles underneath each glomerulus' name represents the "odor scene" of that glomerulus[26,118]. These are: alcoholic fermentation (brown); yeasty (blue); fruity (faded green); decaying fruit (yellow); plant matter (pink); animal matter (pale purple); pheromones (chartreuse); dangerous (red); and, unknown (grey). **(B)** MIPergic LNs do not preferentially innervate glomeruli whose activity has been linked to attractive or aversive behavioral responses ($p = 0.991$, n = 13 ("attractive"), 16 ("aversive"), unpaired t-test with Welch's correction). **(C)** MIPergic LNs do not preferentially innervate glomeruli tuned to any particular odorant molecules ($p = 0.59$, Kruskal-Wallis rank sum test). Odorant molecule functional groups are color coded as follows: terpenes (magenta), ketones (purple), esters (blue), aromatics (aqua marine), amines (chartreuse), aldehydes (green), alcohols (brown), and acids (deep pink). **(D)** The frequency by which a MIPergic LN innervates a glomerulus is not correlated to the volume of the glomerulus (cubic microns). MIPergic LN innervation frequencies are significantly weakly correlated to glomerular volumes delineated by Grabe et al.[156] ($r = 0.35$, $p = 0.018$), but variations in MIPergic innervation frequencies across glomeruli do not correlate (adjusted $R^2 = 0.101$). Conversely, MIPergic LN innervation frequencies do not correlate with projection neuron-based glomerular volumes delineated from electron microscopy data[26,118] ($r = 0.24$, $p = 0.12$). **(E)** Principal components analysis (PCA) of MIPergic LN innervation patterns, where each data point represents MIPergic LN innervation patterns for each glomerulus. Bar graph represents the percentage of the variance explained by each principal component. In all cases, boxplots display the minimum, 25th-percentile, median, 75th-percentile, and 'maximum' of the given data.

Figure S3 Sister MIPergic LN and individual MIPergic LN connectivity dynamics. **(A & B)** On average, ~12 glomeruli are co-innervated by sister MIPergic LN clones. In these examples, two distinct MIPergic LNs co-innervate DL2d and DP1l (respectively). For comparing sister MIPergic LN co-innervation patterns, n = 5 brains; 5 sister clones per brain. **(C-E)** Individual MIPergic LNs innervate thermo-/hygrosensory glomeruli. Branching from an individual MIPergic LN was observed invading the VP4 (formerly, "the arm"), VP3, VP2, and VP1 (formerly, "the column"). VP2-4 are designated by the hatched outline, while an arrowhead designates VP1. **(F-I)** DenMark, synaptotagmin-eGFP (syt.eGFP), and anti-myoinhibitory peptide immunoreactive puncta (anti-MIP) voxel density generally scale with MIPergic LN total cable voxel density within glomeruli. DenMark variations across glomeruli are significantly weakly correlated to the voxel density of total MIPergic LN cable within each glomerulus ($r = 0.38$, $p = 0.0098$). However, variations in DenMark voxel density across glomeruli do not correlate (adjusted $R^2 = 0.12249$). Synaptotagmin-eGFP and anti-MIP voxel density are significantly correlated with the voxel density of total MIPergic LN neurite volume (syt.eGFP: $r = 0.75$, $p = 1.8\text{x}10^{-9}$; anti-MIP: $r = 0.74$, $p = 5.1\text{x}10^{-9}$). The density of syt.eGFP and anti-MIP immunoreactive punctate are significantly correlated ($p = 0.0091$), but variations in either indicator across glomeruli are not (adjusted $R^2 = 0.20567$). In all cases, each data point represents the normalized mean indicator density within a given glomerulus and each line represents the linear regression model. **(J)** All putMIP LNs are synaptically connected to each other. Table of the number of synapses from one putMIP LN to all other putMIP LNs. **(K)** The amount of putative

MIPergic LN reciprocal connectivity assessed within each glomerulus. Heatmap of the amount of input a given putMIP LN (x-axis) receives from all other putMIP LNs within every AL glomerulus as a function of the total amount of input that putMIP LN receives within a glomerulus. In all cases: neuropil was delineated by anti-DN-Cadherin staining; all scale bars = 10um.

Figure S4 SPR-GAL4::VP16 and SPR-T2A-GAL4 expression throughout all primary sensory neurons. **(A)** Expression patterns of the bacterial artificial chromosome derived element SPR-GAL4::VP16 (cyan) and a CRISPR-Cas9 T2A-GAL4 insertion in the coding-intron of the sex peptide receptor (SPR-T2A-GAL4, magenta) in all sensory afferents in mated females, virgin females, and males. The left most diagram represents imaging plane for all images to the right, wherein: **1-1'''''** = auditory afferents; **2-2'''''** = olfactory, thermal, and hygrosensory afferents; **3-3'''''** = olfactory afferents; **4-4'''''** = gustatory afferents; **5-5'''** = visual afferents; **6-6'''** = proprioceptive and gustatory afferents. Driver expression in visual afferents and proprioceptive/gustatory afferents (in T1) were only tested for SPR-T2A-GAL4. Arrowhead(s) in **2-2'''** and **4-4'''** highlight the few neurons the express SPR-GAL4::VP16 in the 3rd-antennal segment (olfactory, thermal, and hygrosensory afferents), and the labellum (gustatory afferents), respectively. Neuron(s) that innervate the sacculus, a thermal/hygrosensory organ in the 3rd-antennal segment, are presented in the insets in the top right of **2-2'''''**. In all cases, scale bar = 10um.

Figure S5 SPR-GAL4::VP16 expression throughout central brain circuitry with emphasis on AL expression. **(A)** Sex peptide receptor expression (SPR; cyan) as revealed using a bacterial artificial chromosome derived GAL4::VP16 element[82]. Note that this element contains the SPR locus and much of the surrounding genomic locus (≈88kb total), and the GAL4::VP16 coding sequence was later inserted before the SPR stop site[82]. This element was then reintroduced at the attp40 landing site[82]. **(B-D)** SPR-GAL4::VP16 expression (cyan) in OSNs housed in the 3rd-antennal segment and maxillary palp. Female mating status does not affect the number of SPR-GAL4::VP16^{+} cells in antennae (p = 0.63; Holm-adjusted Dunn test), but males have significantly more SPR-GAL4::VP16^{+} cells in their antennae than virgin females (p = 0.05; Holm-adjusted Dunn test). However, the number of SPR-GAL4::VP16^{+} cells in the maxillary palp does not differ based on sex or mating status (p = 0.59; Kruskal-Wallis rank sum test). The discrepancy in the number of neurons of a given type observed between the SPR-T2A-GAL4 **(see Figure 5C & 5D)** versus the SPR-GAL4::VP16 drivers is likely a result of the non-native chromosomal topology, as well as potentially missing enhancer elements, of the SPR-GAL4::VP16 driver. **(E)** SPR-GAL4::VP16 (cyan) colocalizes with the general glial marker *reverse polarity* (anti-REPO; yellow). **(F)** SPR-GAL4::VP16 stochastic labeling highlights several glial subtypes, including cortical, neuropil ensheathing, and tract ensheathing glia. **(G)** Several ventral AL neurons are labeled through intersectional genetics experiments between an EGFP-insertion in the endogenous non-coding intron of SPR (MiMIC Cassette; magenta) and SPR-GAL4::VP16 (cyan). **(H)** At least a portion of the ventral AL neurons labeled by SPR-GAL4::VP16 are ventral glutamatergic LNs. The number of vesicular glutamate transporter-positive (VGlut^{+}) SPR-GAL4::VP16 neurons does not statistically differ based on sex or mating status (p = 0.28, n = 8 (virgin females), 7 (mated females), and 8 (males); Kruskal-Wallis rank sum test). **(I)** SPR-GAL4::VP16 stochastic labeling confirms expression in ventral LNs, at least one lateral LN, and at least one ventral multiglomerular PN could be resolved. **(J)** Skeleton representation of the aforementioned SPR-GAL4::VP16 multiglomerular PN. In all cases: neuropil was delineated with anti-DN-cadherin staining; all scale bar = 10um.

Figure S6 Sex peptide receptor (SPR) expression in independently generated projection neuron single-cell RNA-sequencing (scRNA-seq) datasets. **(A)** T-distributed stochastic neighbor embedding (tSNE) plot showing SPR expression (log-transformed and counts per million (CPM) normalized), wherein higher transcript levels are deeper magenta. **(B)** Heatmap showing transcript levels of anterodorsal projection neuron (adPN) marker genes (*acj6* and *kn*), lateral projection neuron (latPN) marker genes (*vvl* and *unpg*), ventral projection neuron (vPN) marker genes (*lim1* and *gad1*), choline acetyltransferase (*ChAT*), vesicular glutamate transporter (*vglut*), and SPR in olfactory projection neuron (OPN) clusters previously identified[85]. **(C)** As in **(A)**, visualization of SPR expression in Croset et al.[84] scRNA-seq dataset. **(D)** As in **(B)**, heatmap showing transcript levels of various genes in OPN clusters previously identified[84]. **(E)** As in **(A)**, visualization of SPR expression in Li et al.[83] OPN scRNA-seq data. **(F)** As in **(B)**, heatmap representation of transcript levels within adPN (OPN 1) and latPN (OPN 2) scRNA-seq clusters. Cluster boundaries were previously identified[83]. In all cases: Transcript levels are CPM normalized and log-transformed.

Figure S7 Generation of a sex peptide receptor (SPR) LexA::QFAD driver line via dual microinjection of a Trojan exon construct and ΦC31 recombinase. **(A)** Schematic representation of MiMIC cassette exchange for LexA::QFAD Trojan exon cassette, and subsequent LexA::QFAD expression in all cells that produce the sex peptide receptor (SPR). **(B)** Crossing scheme used to establish SPR^{MI13553}-T2A-LexA::QFAD transgenics. **(C)** SPR^{MI13553}-T2A-LexA::QFAD expression (cyan) in

the larval central brain and ventral nerve cord. **(D)** $SPR^{MI13553}$-T2A-LexA::QFAD expression (cyan) in the adult central brain. Note that while soma labeled by this driver are faintly reliably resolvable, neural processes are generally unresolvable in the adult. In all cases, scale bars = 10um.

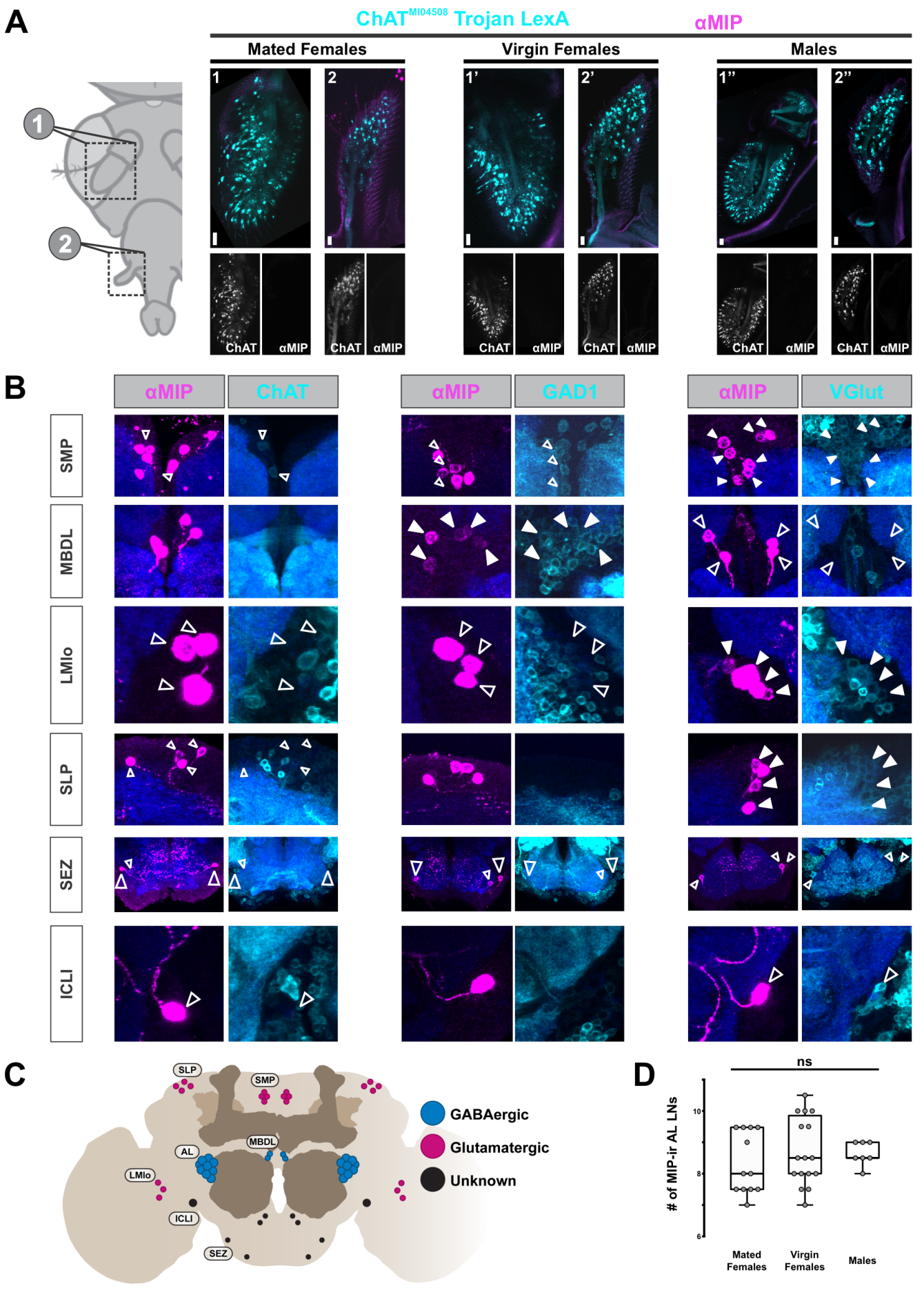

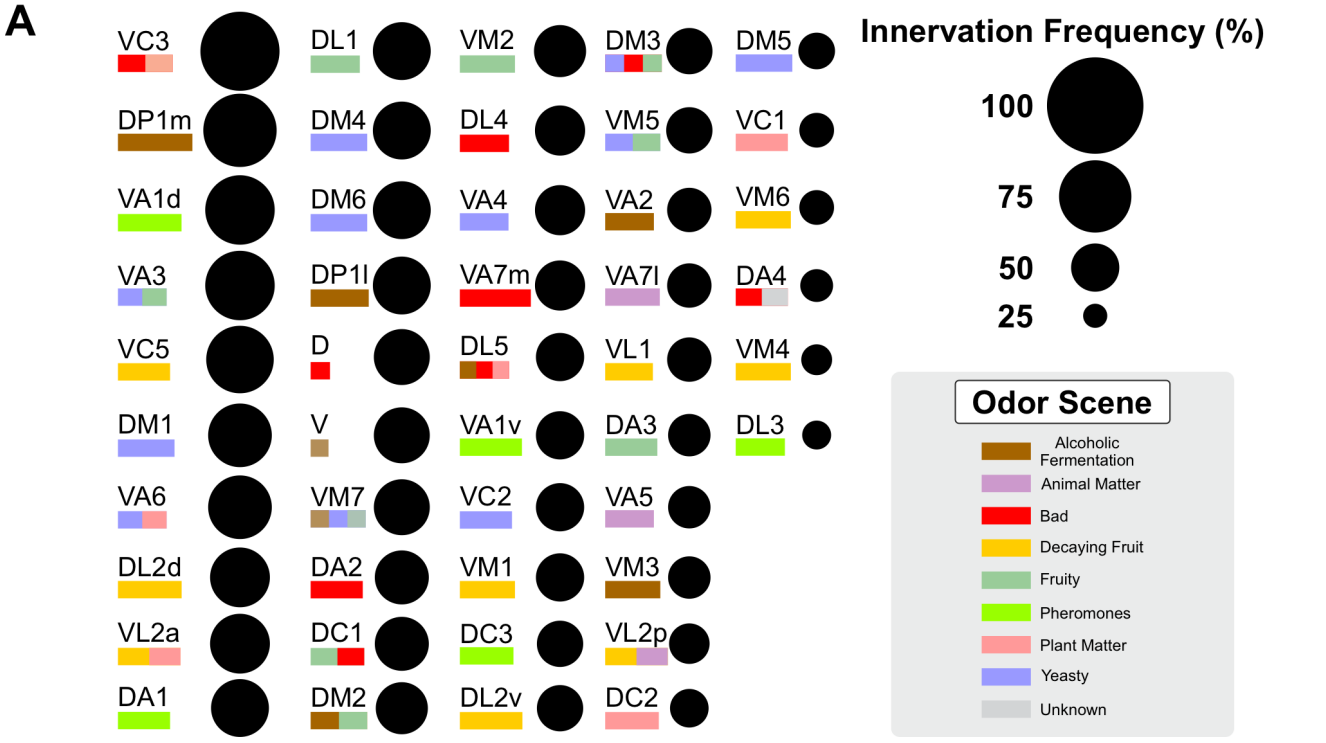

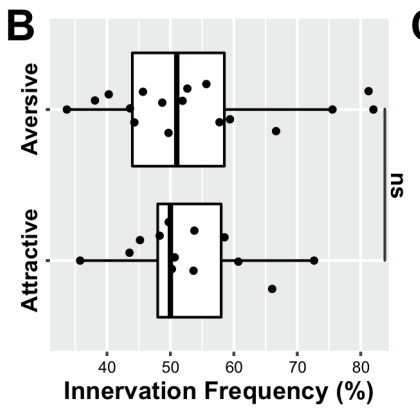

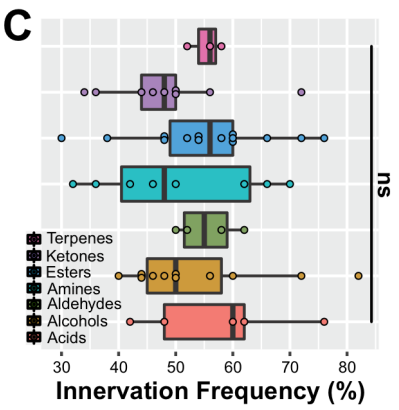

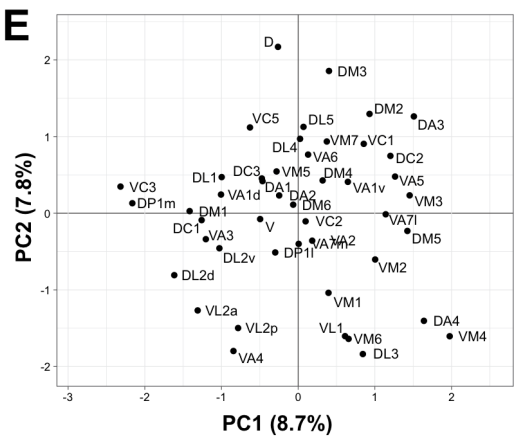

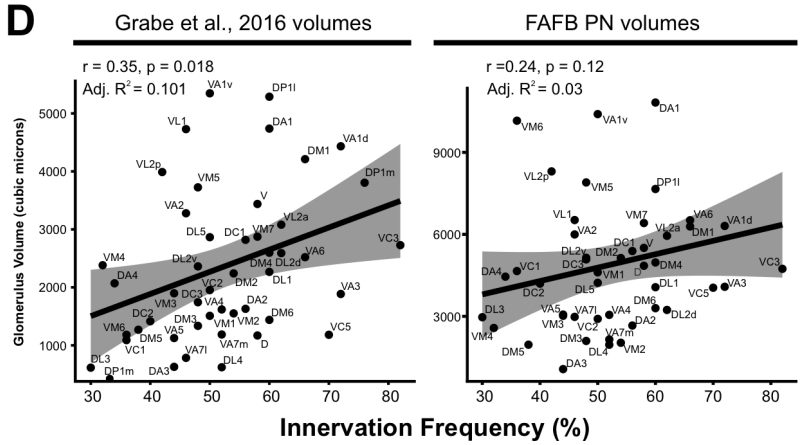

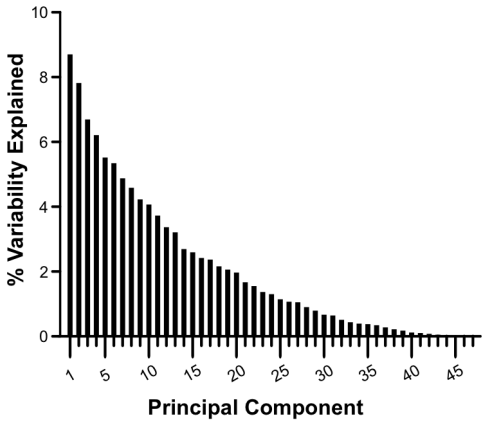

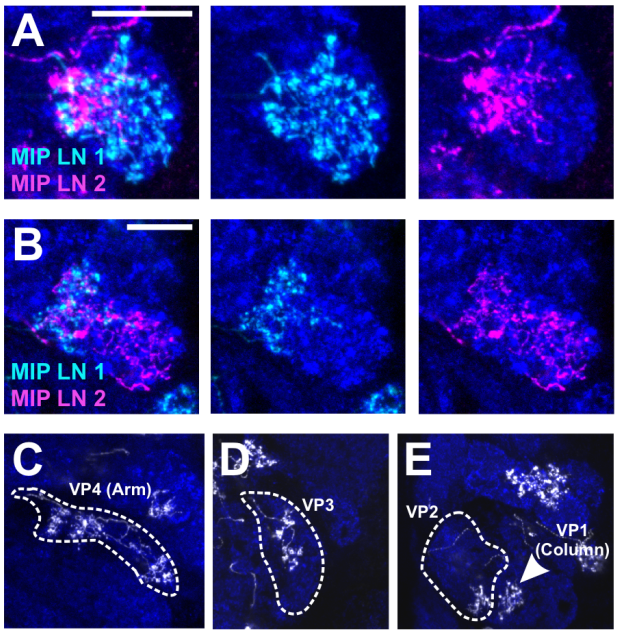

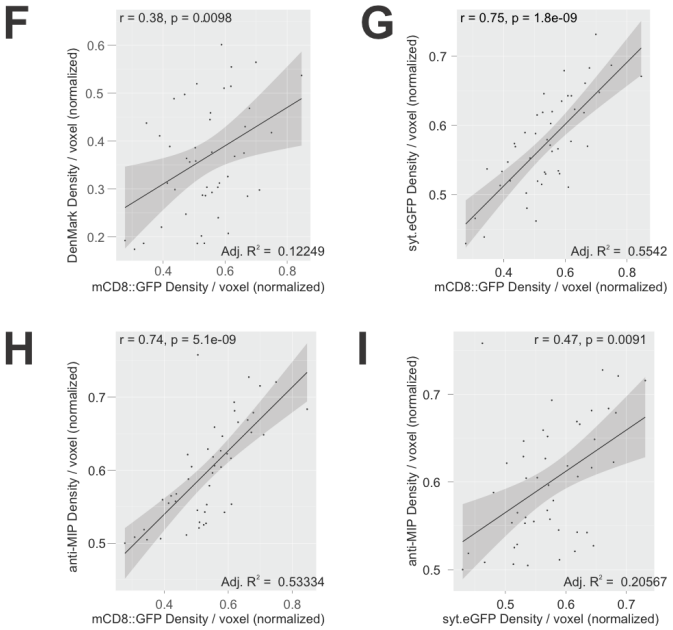

J

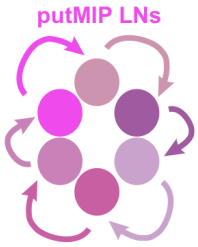

MIP LN 1	MIP LN 2	MIP LN 3	MIP LN 4	MIP LN 5	MIP LN 6	MIP LN 7	MIP LN 8	MIP LN 9	MIP LN 10	MIP LN 11	MIP LN 12	MIP LN 13	MIP LN 14	MIP LN 15	MIP LN 16	MIP LN 17	MIP LN 18	MIP LN 19	MIP LN 20
	216	163	7	11	20	137	24	34	8	47	15	7	27	22	8	24	6	30	40
178		142	16	26	24	145	28	41	11	41	30	9	38	18	6	26	11	18	44
192	172		11	19	22	209	21	32	10	62	23	5	55	31	6	17	12	32	32
18	15	20		122	68	27	11	42	167	42	65	142	46	144	124	84	6	29	27
25	38	21	371		91	26	166	824	75	717	57	82	773	67	55	96	422	175	930
33	30	47	31	45		58	18	35	64	55	13	47	79	38	59	56	19	22	47
197	169	194	11	20	35		23	31	9	66	23	6	55	29	6	24	13	24	41
24	30	20	58	135	32	36		150	37	68	30	28	59	30	19	112	43	29	196
60	45	26	89	330	62	37	119		97	229	65	78	231	107	82	355	102	206	26
4	0	0	32	55	18	2	14	17		140	19	0	125	4	2	47	44	14	18
142	116	102	17	129	27	133	27	63	146		47	66	8	121	77	143	22	34	104
47	34	50	33	46	11	65	22	34	84	73		74	76	35	51	49	27	24	42
1	2	0	22	38	18	3	11	11	0	73	29		107	8	0	36	19	5	13
110	104	95	27	139	46	140	22	84	143	10	41	99		89	95	143	40	31	113
37	42	42	38	74	65	48	27	167	56	38	49	71	54		67	81	41	107	162
2	2	2	32	45	24	2	8	18	0	107	19	0	107	9		32	30	12	18
18	35	19	397	141	91	22	179	888	100	730	91	66	787	45	70		452	181	1015
30	19	25	8	78	62	31	14	33	149	46	51	107	36	182	123	115		29	52
52	37	60	34	136	62	55	24	349	56	65	37	52	62	54	75	112	28		357
54	60	30	98	340	72	42	131	27	114	216	61	98	217	102	70	394	102	230	

K